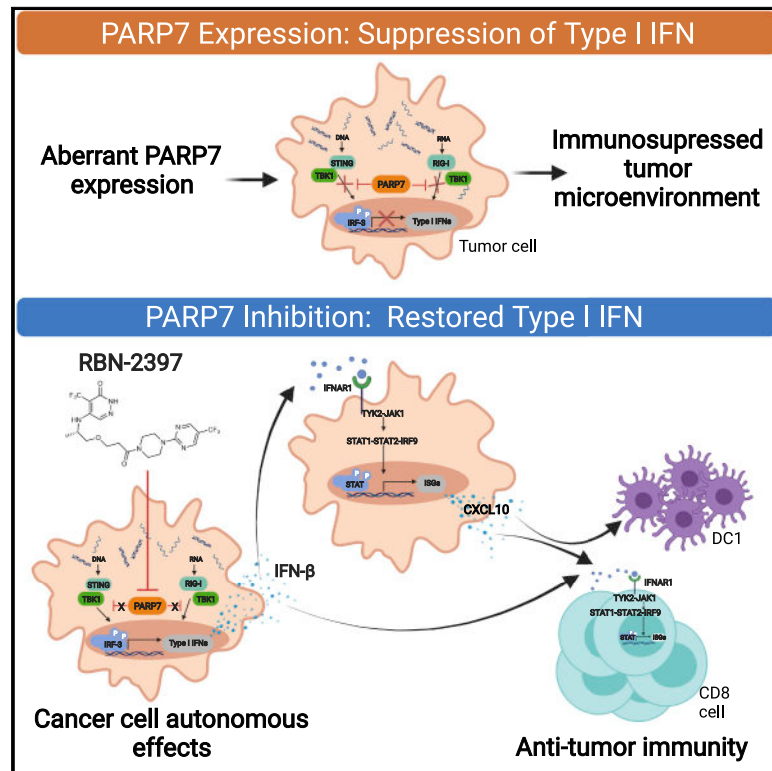


Cancer Cell

PARP7 negatively regulates the type I interferon response in cancer cells and its inhibition triggers antitumor immunity

Graphical abstract



Authors

Joseph M. Gozgit,
Melissa M. Vasbinder, Ryan P. Abo, ...,
Kevin W. Kuntz, Victoria M. Richon,
Heike Keilhack

Correspondence

jgozgit@ribontx.com (J.M.G.),
hkeilhack@ribontx.com (H.K.)

In brief

Engaging cytosolic nucleic acid sensing and the type I interferon (IFN) response is an emerging therapeutic strategy in oncology. Gozgit et al. find that PARP7 is a cancer-specific brake on this pathway and that inhibition of PARP7 by a selective inhibitor, RBN-2397, induces both cancer cell-autonomous effects and antitumor immunity via enhanced IFN signaling.

Highlights

- PARP7 acts as a brake in cytosolic nucleic acid sensing in a TBK1-dependent manner
- RBN-2397 is a potent and selective PARP7 inhibitor targeting this cancer vulnerability
- RBN-2397 restores the type I interferon (IFN) response in tumor cells
- RBN-2397 induces antitumor immunity dependent on type I IFN and CD8 T cells



Article

PARP7 negatively regulates the type I interferon response in cancer cells and its inhibition triggers antitumor immunity

Joseph M. Gozgit,^{1,4,5,*} Melissa M. Vasbinder,^{1,4} Ryan P. Abo,¹ Kaiko Kunii,¹ Kristy G. Kuplast-Barr,¹ Bin Gui,¹ Alvin Z. Lu,¹ Jennifer R. Molina,¹ Elena Minissale,¹ Kerren K. Swinger,¹ Tim J. Wigle,¹ Danielle J. Blackwell,¹ Christina R. Majer,¹ Yue Ren,¹ Mario Niepel,¹ Zacharenia A. Varsamis,¹ Sunaina P. Nayak,¹ Ellen Bamberg,¹ Jan-Rung Mo,¹ W. David Church,¹ Ahmed S.A. Mady,¹ Jeff Song,¹ Luke Utley,¹ Patricia E. Rao,² Timothy J. Mitchison,³ Kevin W. Kuntz,¹ Victoria M. Richon,¹ and Heike Keilhack^{1,*}

¹Ribon Therapeutics, 35 Cambridgepark Drive, Suite 300, Cambridge, MA 02140, USA

²Patricia E. Rao Consulting, Acton, MA 01720, USA

³Department of Systems Biology, Harvard Medical School, 200 Longwood Avenue, Warren Alpert 536, Boston, MA 02115, USA

⁴These authors contributed equally

⁵Lead contact

*Correspondence: jgozgit@ribontx.com (J.M.G.), hkeilhack@ribontx.com (H.K.)

<https://doi.org/10.1016/j.ccell.2021.06.018>

SUMMARY

PARP7 is a monoPARP that catalyzes the transfer of single units of ADP-ribose onto substrates to change their function. Here, we identify PARP7 as a negative regulator of nucleic acid sensing in tumor cells. Inhibition of PARP7 restores type I interferon (IFN) signaling responses to nucleic acids in tumor models. Restored signaling can directly inhibit cell proliferation and activate the immune system, both of which contribute to tumor regression. Oral dosing of the PARP7 small-molecule inhibitor, RBN-2397, results in complete tumor regression in a lung cancer xenograft and induces tumor-specific adaptive immune memory in an immunocompetent mouse cancer model, dependent on inducing type I IFN signaling in tumor cells. PARP7 is a therapeutic target whose inhibition induces both cancer cell-autonomous and immune stimulatory effects via enhanced IFN signaling. These data support the targeting of a monoPARP in cancer and introduce a potent and selective PARP7 inhibitor to enter clinical development.

INTRODUCTION

Poly[adenosine diphosphate (ADP)-ribose] polymerases (PARPs) are members of a family of 17 enzymes that regulate fundamental cellular processes including gene expression, protein degradation, and multiple cellular stress responses (Cohen and Chang, 2018). The ability of cancer cells to survive under stress is a fundamental cancer mechanism and an emerging approach for therapeutics (Luo et al., 2009). PARPs use nicotinamide adenine dinucleotide (NAD⁺) to post-translationally modify substrate proteins with ADP-ribose, a process referred to as ADP ribosylation. The majority of PARP family members are referred to as monoPARPs, because they catalyze the transfer of a single unit of ADP-ribose (i.e., mono[ADP-ribose] or MAR) onto their substrates (MARylation), while other polyPARPs attach polymers of ADP-ribose units (i.e., poly[ADP-ribose] or PAR) onto their substrates (PARylation). One member of the polyPARP subfamily, PARP1, has already been shown to be an effective cancer target in connection with cellular stress induced by DNA damage, induced either by genetic mutation or by cytotoxic chemotherapy, with four approved drugs on the market and several others in the late stage of development (Ohmoto and Yachida, 2017).

In contrast to PARP1, PARP7 (TIPARP) is a monoPARP whose expression is upregulated by ligands of the aryl hydrocarbon receptor (AHR), including chemicals found in cigarette smoke (Matthews, 2017). PARP7 acts as a negative feedback mechanism to regulate the expression of cytochrome P450 genes, CYP1A1 and CYP1B1 (MacPherson et al., 2013, 2014). In the context of viral infection, AHR-induced PARP7 can interact with TBK1, a major kinase that is activated during the onset of pathogen-associated molecular pattern pathways leading to an activation of the type I interferon (IFN) response and antiviral immunity (Yamada et al., 2016). PARP7 was shown to MARYlate TBK1, which prevents its activation, thereby repressing the type I IFN response. Based on these results after viral infection, one could hypothesize that cancer cells can use aberrantly expressed and/or activated PARP7 as a mechanism to evade the host immune system through suppression of the type I IFN response and thereby T cell-mediated antitumor immunity. In a recent genetic screen to identify tumor factors that suppress T cell activation, PARP7 was identified as a significant gene hit (Pan et al., 2018). PARP7 knockout in a mouse melanoma cell line was shown to increase the proliferation and activation of co-cultured T cells, suggesting that PARP7



inhibition may be a viable strategy to activate T cell-mediated tumor killing.

Pattern recognition receptor (PRR) pathways, including sensing mechanisms through cGAS/STING and RIG-I, activate type I IFNs to induce innate immunity in response to pathogen- or damage-generated cytosolic nucleic acids (Ivashkiv and Donlin, 2014; Paludan et al., 2019; Barber, 2015; Ishikawa and Barber, 2008; Ahn et al., 2014; Hartlova et al., 2015). For instance, interaction of cytosolic DNA with cGAS activates the synthesis of the second messenger, cGAMP, leading to conformational changes in STING and phosphorylation of TBK1. Activated TBK1 in turn phosphorylates IRF3, leading to the transcription of type I IFN genes (Borden, 2019). Type I IFNs bind the IFN- α/β receptor (IFNAR) and signal through the JAK/STAT pathway (Majoros et al., 2017), leading to the expression of hundreds of IFN-stimulated genes (ISGs) (Borden, 2019) that regulate diverse cellular functions in response to sensing cytosolic nucleic acids. Due to genomic instability, cancer cells often harbor aberrant cytosolic nucleic acids, which can activate PRRs (Paludan et al., 2019; Hatch et al., 2013; Harding et al., 2017; Mackenzie et al., 2017; Gluck et al., 2017). The resulting inflammatory signaling could favor cancer growth at low levels and trigger cell death or immune recognition at high levels (Cheon et al., 2014), suggesting that cancer cells are under selective pressure to regulate signaling strength. Here, we identify PARP7 as a negative regulator of nucleic acid sensing whose expression is upregulated in cancer to preferentially downregulate IFN signaling. PARP7 inhibitors can unleash tumoral IFN signaling, leading to tumor regression and durable immunity.

RESULTS

RBN-2397 is a potent inhibitor of PARP7 that restores type I IFN signaling

In primary tumors of squamous histology, the *PARP7* gene locus region on chromosome 3 (3q25) is frequently amplified, corresponding to increased levels of *PARP7* mRNA expression levels (Figures S1A and S1B; www.cancer.gov/tcga). As PARP7 has been shown to suppress virus-induced type I IFN signaling, we assessed the relationship between PARP7 expression and baseline IFN gene expression using a published ISG score (Liu et al., 2019). We found that PARP7 expression is significantly correlated with ISG score in most cancer types (Figure S1C). To understand whether cancer cells depend on PARP7 for proliferation, we investigated PARP7 in publicly available CRISPR screening databases (www.depmap.org). These analyses revealed that a subset of cancers exhibit PARP7 dependency. Importantly there is no correlation observed between PARP7 and PARP1 CRISPR dependencies in cancer cell lines (Figure S1D). Furthermore, higher PARP7 expression corresponds with higher PARP7 cell line dependency (Figure S1E). These data suggest that a subset of cancers distinctly depend on PARP7 compared with PARP1 and support PARP7 as a putative cancer target.

As part of our drug-discovery efforts to identify potent and selective inhibitors of PARP7, we utilized structure-based design to optimize an unselective monoPARP inhibitor identified by screening Ribon's internal compound collection of PARP inhibitors. Further optimization of potency, selectivity, and physicochemical properties led to the discovery of RBN-2397, a small-

molecule potent and selective inhibitor of PARP7 catalytic function (Figures 1A and S2A; Table S1). A co-crystal structure of RBN-2397 demonstrated binding in the NAD⁺-binding pocket (Figure 1B). In contrast to the approved PARP1 inhibitors, RBN-2397 uniquely inhibits PARP7 within the family of human PARPs with catalytic activity, as measured by biochemical enzyme inhibition or biophysical assays (Figures 1C and S2A). RBN-2397 inhibits PARP7 with an IC₅₀ of <3 nM in a probe displacement assay and has a K_D of 0.22 nM measured using surface plasmon resonance (Figures 1C, S2A, and S2B), demonstrating >50-fold selectivity for inhibition of PARP7 over all PARP family members (Wigle et al., 2020a, 2020b). Binding to PARP7 in the cellular milieu was shown by its ability to displace an active-site probe in a NanoBRET assay, where RBN-2397 exhibited dose-dependent inhibition of the BRET signal with an IC₅₀ of 1 nM, demonstrating 500-fold selectivity for PARP7 over PARP12, another monoPARP that is structurally similar to PARP7 (Figure S2C). The inhibition of PARP1-mediated ADP ribosylation has been well characterized for several PARP1 inhibitors using a cellular PARylation assay (Jones et al., 2015; Wang et al., 2016). We have previously shown that while PARP1 inhibitors potently inhibit PARylation, these compounds show little to weak inhibition of cellular MARYlation (Lu et al., 2019). Here we show that RBN-2397 inhibits MARYlation of multiple intracellular proteins in PARP7-overexpressing SK-MES-1 cells with an IC₅₀ of 2 nM, showing a 300-fold window over the inhibition of PARylation in PARP1-activated HeLa cells (Figure 1D). It was previously shown that PARP7 selectively acts as a negative feedback mechanism to regulate the expression of *CYP1A1* and *CYP1B1* genes (MacPherson et al., 2013, 2014). RBN-2397 treatment increased expression of *CYP1B1* mRNA in HARA cells in a single-plex assay (Figure S2D) and in NCI-H1373 and NCI-H647 cells demonstrated by RNA sequencing (Table S2), consistent with release from the negative regulatory effect of PARP7 on AHR-driven transcription. Together, these data suggest that RBN-2397 is a highly selective and cell-potent PARP7 inhibitor leading to on-target pharmacological effects in cells.

PARP7 was reported to suppress the IFN response to both viral DNA and synthetic RNA by interacting with TBK1 and suppressing its activity by ADP ribosylation (Yamada et al., 2016). We confirmed that overexpression of PARP7 can suppress the IFN response to synthetic double-stranded DNA, poly(dA:dT), as measured by a decrease in *IFN- β* mRNA levels in HEK293T cells (Figure 1E). We next demonstrated that PARP7-dependent MARYlation of recombinant TBK1 is completely abolished by RBN-2397 (Figure S2E). To further evaluate the effects of PARP7 inhibition on type I IFN signaling in the context of cancer, we screened a panel of mouse cancer cell lines (Figures S3A and S3B) and found that RBN-2397 restored type I IFN signaling in CT26 cells as measured by a concentration-dependent increase in STAT1 phosphorylation and *CXCL10* mRNA levels (Figures 1F and 1G). RBN-2397 did not affect the proliferation of CT26 cells at concentrations up to 10 μ M (Figures S3A and S3B). The specificity of RBN-2397 for restoring the type I IFN response in CT26 cells was assessed using an inactive but structurally related analog of RBN-2397, RBN250036, which is methylated at a key nitrogen in the nicotinamide-binding pocket, resulting in the loss of activity against all PARP family members (Figures S3C and S3D). RBN250036 had no effect on pSTAT1 and

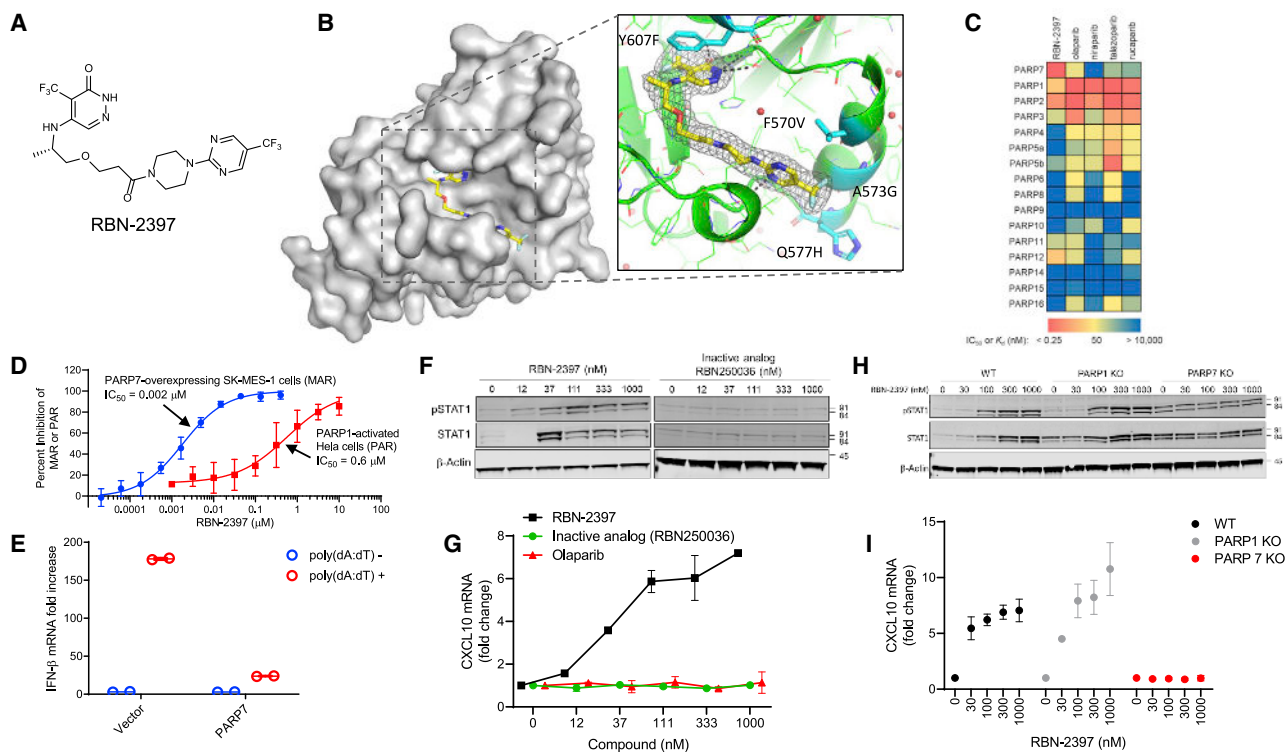


Figure 1. RBN-2397 is a potent inhibitor of PARP7 that restores type I IFN signaling

(A) Structure of RBN-2397.

(B) Crystal structure of PARP12 protein that has been mutated to resemble PARP7 shown as surface representation with enhanced view of the active site shown as ribbon diagram (green, mutations in cyan), RBN-2397 (yellow) at 2.0 Å with 2F_o-F_c electron density map (1σ, white mesh), and hydrogen bonds (dashes). PARP12 was used as a surrogate, since PARP7 protein did not crystallize; four key residues were mutated to match the PARP7 sequence (cyan).

(C) Selectivity of RBN-2397 in biochemical enzyme inhibition or biophysical assays (see Figure S2A for further information).

(D) RBN-2397 potently inhibits MARYlation in SK-MES-1 cells compared with PARYlation in PARP1-activated HeLa cells. Data shown as mean ± SD from two experiments tested in at least duplicate.

(E) Expression of *IFN-β* mRNA in HEK293T cells treated with poly(dA:dT) in the presence of PARP7 overexpression. Representative data shown from a single experiment, experiment repeated twice.

(F) Concentration-dependent increase in pSTAT1 by RBN-2397 compared with an inactive analog, RBN250036, in CT26 cells. Representative data shown from a single experiment, experiment repeated twice.

(G) Effects of RBN-2397 on *CXCL10* mRNA compared with an inactive analog, RBN250036, and PARP1 inhibitor, olaparib, in CT26 cells. Representative data shown as mean ± SD, n = 2, experiment repeated twice.

(H) Changes in pSTAT1 by RBN-2397 in wild-type (WT) CT26 cells, and PARP1 KO or PARP7 KO CT26 stable clones. Representative data shown from a single experiment, experiment repeated twice.

(I) Changes in *CXCL10* mRNA by RBN-2397 in wild-type (WT) CT26 cells, and PARP1 KO or PARP7 KO CT26 clones. Representative data shown as mean ± SD, n = 2, experiment repeated twice. Vehicle-treated PARP7 KO cells showed 2.4-fold increase in *CXCL10* mRNA levels compared with vehicle-treated WT CT26 cells.

CXCL10 in CT26 cells (Figures 1F and 1G), demonstrating that RBN-2397 restores the type I IFN response by specifically inhibiting PARP7 catalytic activity. We next assessed the effects of the PARP1 inhibitor olaparib on the type I IFN response and showed that inhibition of PARP1 did not increase STAT1 phosphorylation (Figure S3E) or *CXCL10* (Figure 1G) in CT26 cells. To further examine the on-target activity of RBN-2397, we used CRISPR/Cas9 to knock out selected PARP family members. Stable knockout (KO) of PARP7 prevented any additional increase of STAT1 phosphorylation or *CXCL10* mRNA by RBN-2397 in CT26 cells; however, KO of PARPs 1, 2, 3, or 12 had no effect on the induction of type I IFN signaling by RBN-2397 (Figures 1H, 1I, S4A, and S4B). The double KO of PARP1 and PARP2 (PARP1/2) showed a result similar to that for single-KO

cells (Figures S4A and S4B). These data suggest that activation of the type I IFN response by RBN-2397 is an on-target effect of inhibiting PARP7.

RBN-2397 induces antitumor immunity dependent on CD8 T cells

To investigate the role of PARP7 in the antitumor immune response *in vivo*, we orally dosed CT26 tumor-bearing, immunocompetent BALB/c mice on a continuous daily schedule with vehicle or RBN-2397 (3–100 mg/kg once daily [QD]) or using an intermittent schedule of 5 days on and 2 days off (100 mg/kg). RBN-2397 was either administered alone or co-formulated with the cytochrome P450 inhibitor, 1-aminobenzotriazole (1-ABT), to increase mouse exposure (Figures S5B and S5E). RBN-2397

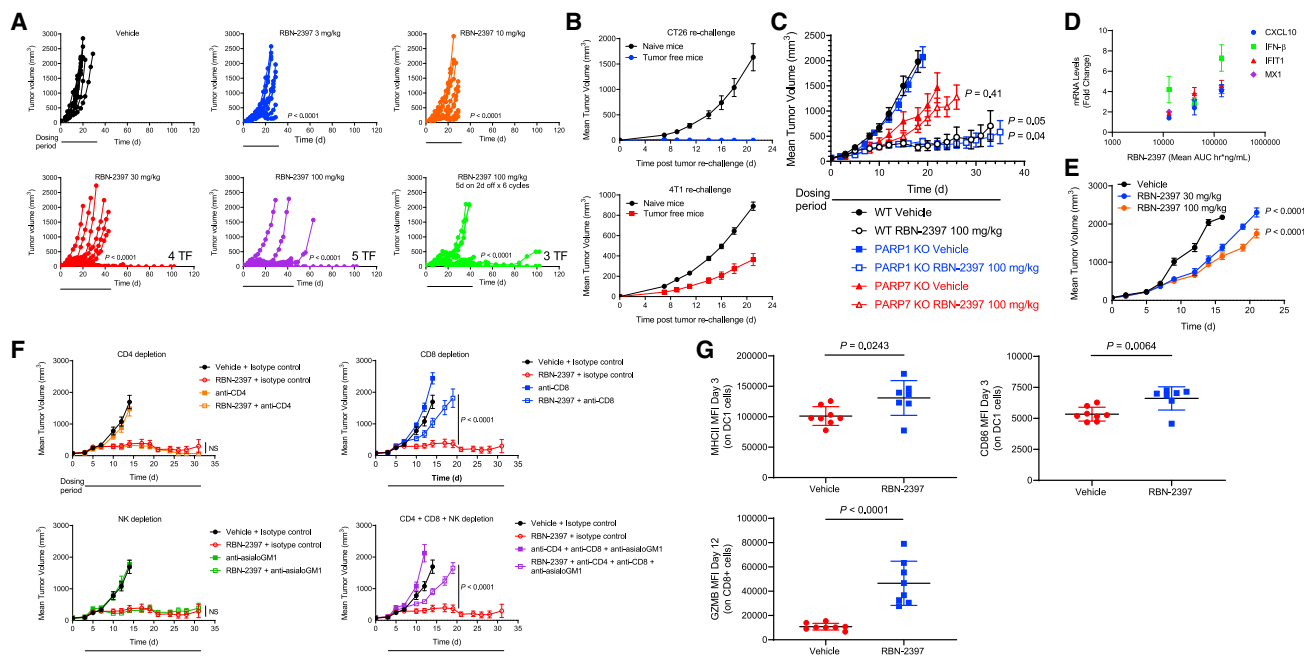


Figure 2. RBN-2397 induces antitumor immunity dependent on CD8 T cells

(A) Antitumor activity of RBN-2397 (QD × 42 days; dosing period indicated by solid line) in CT26 tumor-bearing BALB/c mice (n = 10). Treatment was initiated 6 days after tumor inoculation when mean tumor size reached 54 mm³. p value determined by two-way ANOVA with multiple comparisons on day 18. All mice were co-dosed with 1-ABT. QD, Once daily; TF, tumor-free.

(B) Twelve CT26 tumor-free mice after RBN-2397 treatment were rechallenged with CT26 or 4T1 cells (mean ± SEM, n = 12). Naive mice were used as control (mean ± SEM, n = 8).

(C) Activity of RBN-2397 (QD × 35 days) in CT26 wild-type (WT), PARP1 KO, or PARP7 KO tumor-bearing BALB/c mice (n = 10). Treatment was initiated when mean tumor size reached 61, 65, and 59 mm³ for WT, PARP1 KO, and PARP7 KO, respectively. p value determined by a two-tailed Student's t test (WT day 18, PARP1 KO day 19, and PARP7 KO day 22). Data shown as tumor volume (mean ± SEM) for measurements with ≥ 80% of the mice remaining in the group. All mice were co-dosed with 1-ABT. QD, once daily; TF, tumor-free.

(D) Exposure-dependent increase of tumoral *IFN-β*, *CXCL10*, *IFIT1*, and *MX1* mRNAs in CT26 tumor-bearing mice dosed with RBN-2397. Data are shown as mean ± SD, n = 5, experiment repeated twice with similar results. All mice were co-dosed with 1-ABT.

(E) CT26 tumor-bearing NOG mice (mean tumor size of 69 mm³) were administered either vehicle or RBN-2397 (QD × 21 days, n = 10). p value determined by two-way ANOVA with multiple comparisons on day 14. Data shown as tumor volume (mean ± SEM) for measurements with ≥ 80% of the mice remaining in the group. All mice were co-dosed with 1-ABT.

(F) CT26 tumor-bearing BALB/c mice (mean tumor size of 76 mm³) were administered either vehicle or 100 mg/kg RBN-2397 (QD × 28 days; dosing period indicated by solid line) in the presence of either isotype control, anti-CD4, anti-CD8, or anti-asialoGM1 antibodies (n = 10). p value determined by two-way ANOVA with multiple comparisons on day 19. Data shown as tumor volume (mean ± SEM) for measurements with ≥ 80% of the mice remaining in the group. QD, once daily; NS, not significant. All mice were co-dosed with 1-ABT.

(G) Changes in tumor immune cell populations and activation markers by RBN-2397 dosed at 500 mg/kg in CT26 tumor-bearing mice. Treatment was initiated with mean tumor size of 81 mm³. Data are shown as mean ± SD, n = 8. p value determined by a two-tailed Student's t test.

significantly inhibited tumor growth at all dose levels and schedules, with complete and durable regression observed in 12 mice at doses ≥ 30 mg/kg following 6 weeks of dosing (Figure 2A). After 60 days of follow-up, all 12 tumor-free (TF) mice rejected a challenge of injected CT26 cells, but 11 of the 12 developed 4T1 tumors, demonstrating development of tumor-specific adaptive immune memory (Figure 2B; Corrales et al., 2015). Using CT26 KO cell lines (described in Figures 1H, 1I, S4A, and S4B), we found that PARP2 is indispensable for the immunomodulatory and antitumor effects of RBN-2397 *in vivo* compared with PARPs 1, 2, 3, 12, and 1/2 (Figures 2C and S4C). Administration of RBN-2397 (100 mg/kg) resulted in strong regression of wild-type (WT) and PARP KO (PARPs 1, 2, 3, 12, and 1/2) CT26 tumors with multiple TF mice observed in all groups; however, no regressions were observed in PARP7 KO tumor-bearing mice (Figures 2C and S4C). Enhanced antitumor activity was observed with RBN-2397

in PARP2, 3, 12, and 1/2 KO tumors (Figure S4C). These data further support the on-target immunomodulatory activity of RBN-2397. RBN-2397 showed an exposure-dependent increase in *IFN-β*, *CXCL10*, *MX1*, and *IFIT1* mRNAs in CT26 tumors (Figure 2D) but not in spleen tissue (Figure S5A) from mice administered a single dose, suggesting tumor-specific activation of type I IFN signaling in this model. RBN-2397 exposure levels (Figure S5B) required for antitumor activity coincided with the observable pharmacodynamic effects in the tumor (Figure 2D).

To evaluate whether the adaptive immune response was required for the antitumor effects of RBN-2397, we orally dosed CT26-tumor-bearing immunodeficient NOG mice with RBN-2397. In contrast to the complete and durable regression observed by RBN-2397 in CT26 tumor-bearing BALB/c mice, RBN-2397 showed reduced activity of 49% and 55% tumor growth inhibition (TGI) at 30 and 100 mg/kg, respectively, with

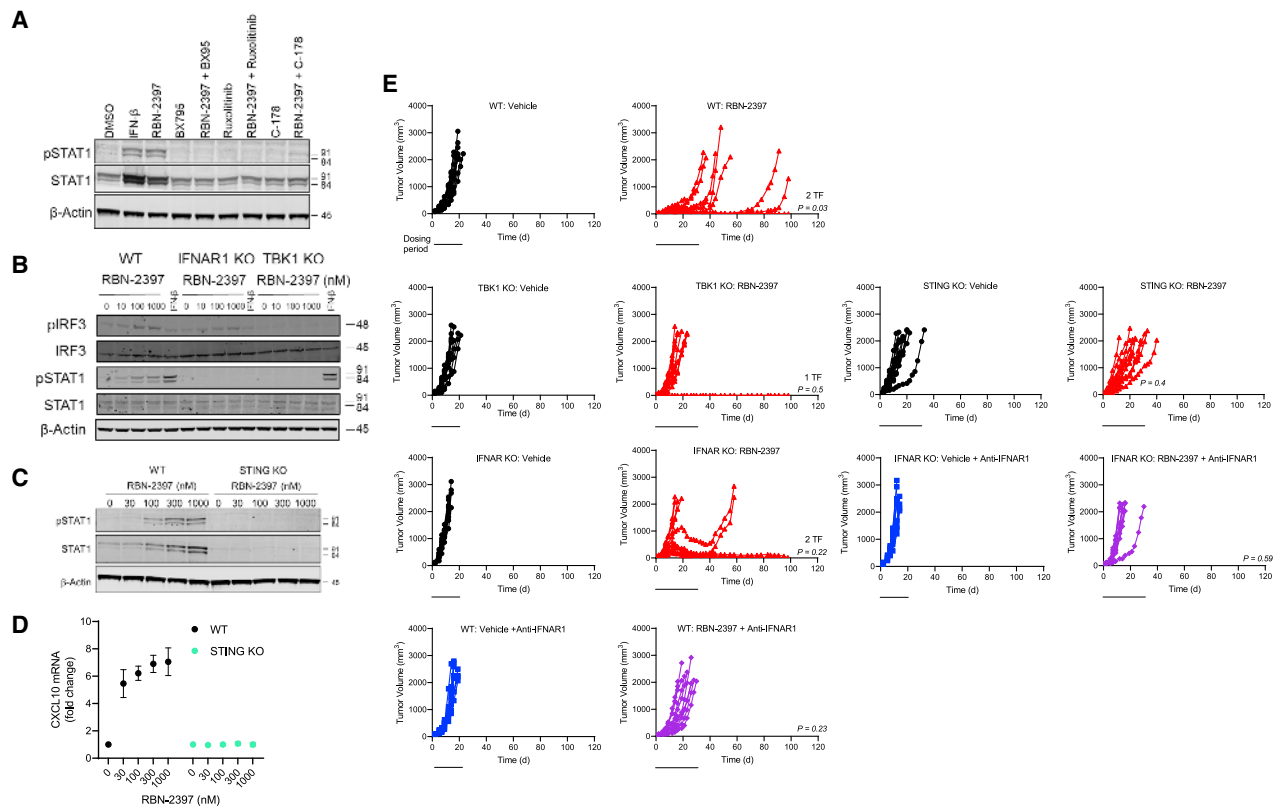


Figure 3. RBN-2397 antitumor immunity is dependent on tumor-produced type I IFN signaling

(A) Effects of TBK1 (BX795), JAK (ruxolitinib), or STING (C-178) blockade on RBN-2397-induced pSTAT1 in CT26 cells. Representative data shown from a single experiment, experiment repeated twice.

(B) Effects of RBN-2397 on pIRF3 and pSTAT1 determined by western immunoblotting in wild-type (WT), TBK1 KO, or IFNAR1 KO CT26 cells following 24-h treatment. Representative data shown from single experiment, repeated twice.

(C) Effects of RBN-2397 on pSTAT1 in WT and STING KO CT26 cells. Representative data shown from single experiment, repeated twice.

(D) Effects of RBN-2397 on CXCL10 mRNA levels in WT and STING KO CT26 cells. Representative data shown from single experiment, repeated twice.

(E) Antitumor activity of 100 mg/kg RBN-2397 (QD × 35 days; dosing period indicated by solid line) in BALB/c subcutaneous tumor model using wild-type (WT), IFNAR1 KO, TBK1, or STING KO CT26 cells. Tumor-bearing mice (mean size of 52, 63, 47 or 65 mm³ for WT, IFNAR1 KO, TBK1 KO, or STING KO tumors, respectively) were dosed orally with vehicle or RBN-2397 alone or in combination with anti-IFNAR1 neutralizing antibody (n = 10). p value determined by a two-tailed Student's t test (WT day 19; IFNAR1 KO, TBK1 KO, and STING KO day 14). All mice were co-dosed with 50 mg/kg 1-ABT. QD, once daily; TF, tumor-free.

no tumor regression (Figure 2E). To assess which immune cell populations are involved in the antitumor effects of RBN-2397, we depleted CT26 tumor-bearing BALB/c mice of CD4 T, CD8 T, or natural killer (NK) cells (Figure S5C). Depletion of CD4 T or NK cells had no effect on RBN-2397 antitumor activity; however, depletion of CD8 T cells significantly reversed the effects of RBN-2397 (Figure 2F), suggesting that CD8 T cells are responsible for much of the antitumor immunity induced by RBN-2397. Depletion of all three cell types showed similar effects as depletion of CD8 T cells alone (Figure 2F). We also assessed the effects of RBN-2397 on tumor-infiltrating immune cell populations by flow cytometry. We found that CT26 tumor-bearing mice dosed daily with 500 mg/kg of RBN-2397 showed significant up-regulation of MHCII, responsible for antigen presentation, and CD86, responsible for delivery of the second activation signal to T cells, on type I dendritic cells (DC1) by day 3 (Figures 2G and S5D). CD8 tumor-infiltrating lymphocytes of RBN-2397-treated mice had significantly increased levels of granzyme B on days 6 and 12, suggesting enhanced cytotoxic ability (Figures

2G and S5D). The exposure levels of 500 mg/kg RBN-2397 (Figure S5E) were in line with levels observed with 30 mg/kg RBN-2397 co-formulated with 1-ABT (Figure S5B). We also observed that RBN-2397 significantly increased the prevalence of systemically distributed tumor antigen-specific T cells as shown by a 1.9-fold increase in the number of splenic T cells producing IFN-γ in response to the CT26 antigen, AH1 (gp70; Figure S5F; Huang et al., 1996). This expansion of reactive cells was tumor specific, as no increase was seen in the number of splenic T cells producing IFN-γ in response to an irrelevant peptide, β-galactosidase peptide (β-gal; Figure S5F; Wang et al., 2018).

RBN-2397 antitumor immunity is dependent on tumor-produced type I IFN signaling

To investigate the mechanism of RBN-2397 in restoring type I IFN signaling, we used pharmacological inhibitors BX795 for TBK1 (Clark et al., 2009), C-178 for STING (Haag et al., 2018), and ruxolitinib for JAK1/2 (Quintas-Cardama et al., 2010; Pattison et al., 2012), and observed that TBK1, STING, and JAK are required

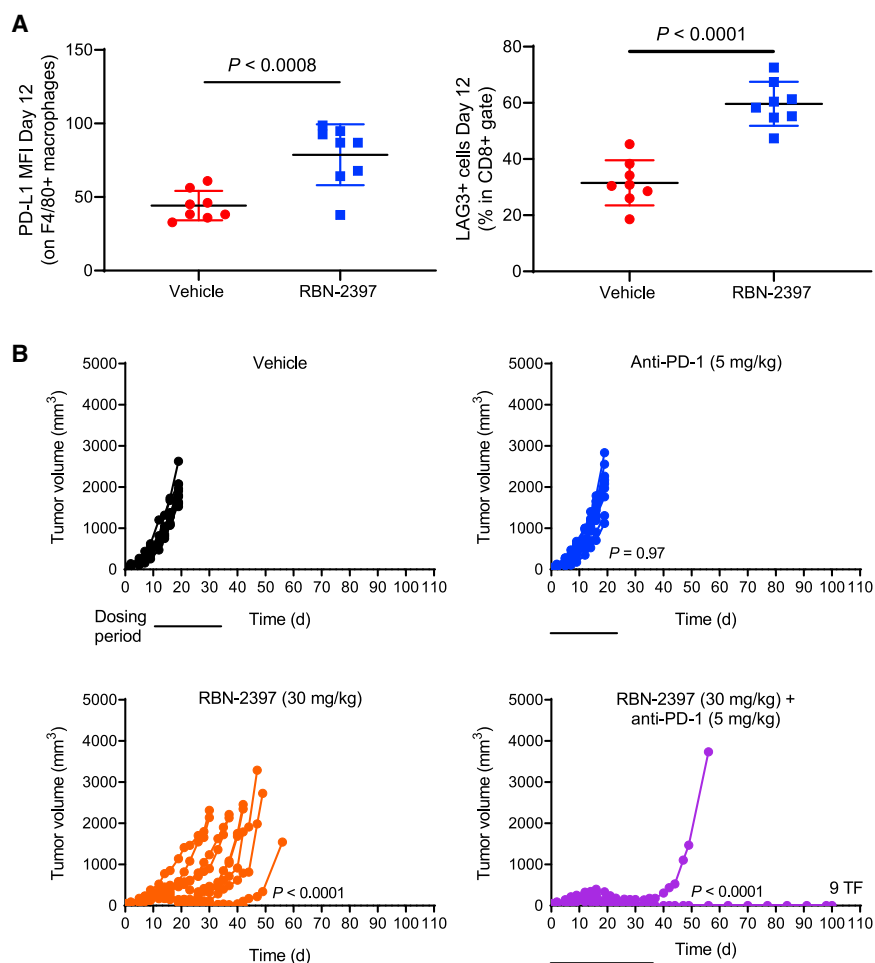


Figure 4. Enhanced antitumor immunity with the combination of anti-PD-1 and RBN-2397

(A) Changes in tumor immune cell populations and activation markers by RBN-2397 dosed at 500 mg/kg in CT26 tumor-bearing BALB/c mice. Data shown as mean \pm SD, $n = 8$. p value determined by a two-tailed Student's t test.

(B) Antitumor activity of RBN-2397 (QD \times 35 days) in combination with anti-PD-1 in CT26 tumor-bearing BALB/c mice (mean tumor size of 54 mm³, $n = 10$). p value determined by two-way ANOVA with multiple comparisons on day 19. All mice were co-dosed with 1-ABT. QD, once daily; TF, tumor-free.

nity is dependent on the effects of tumor-derived IFN on immune cells (Figure 3E). Further supporting this interpretation, administration of the anti-IFNAR1 antibody to mice bearing WT tumors phenocopied the results of the IFNAR1 KO plus anti-IFNAR antibody (Figure 3E). Based on these findings, it appears that tumor-produced type I IFN, induced through inhibition of PARP7 by RBN-2397, plays a major role in the development of durable antitumor immunity in this system.

Enhanced antitumor immunity with the combination of anti-PD-1 and RBN-2397

Using flow cytometry, we observed increases in PD-L1 on macrophages and LAG3 on CD8 T cells, markers of immune

feedback regulation and immune exhaustion, on days 6 and 12, from tumor-infiltrating lymphocytes of mice bearing CT26 tumors treated with 500 mg/kg RBN-2397 (Figures 4A and S5D). Therefore, we next sought to evaluate whether the combination of RBN-2397 with an anti-PD-1 antibody might mitigate PD-L1-mediated inhibition of T cell activity and revive exhausted cytotoxic T lymphocytes, further enhancing antitumor responses (Pardoll, 2012). Given the increase of PD-L1 on myeloid cells in the CT26 tumor microenvironment following dosing with RBN-2397, we started the administration of anti-PD-1 antibody on day 6. RBN-2397 at 30 mg/kg showed significant TGI as a single agent compared with anti-PD-1; however, the combination of anti-PD-1 with RBN-2397 resulted in complete and durable regressions in nine of the ten mice tested (Figure 4B). These data suggest enhanced antitumor immunity with the combination compared with either agent alone when tested at these dose levels.

for the RBN-2397-mediated increase in STAT1 phosphorylation (Figure 3A). To confirm these findings, we used CRISPR/Cas9 to ablate either TBK1, STING, or IFNAR1 from CT26 cells. We found that KO of TBK1 prevents both IRF3 and STAT1 phosphorylation by RBN-2397, whereas KO of IFNAR1 only blocks RBN-2397-induced STAT1 phosphorylation (Figure 3B). Likewise, the type I IFN response by RBN-2397 was diminished in STING KO cells, demonstrated by abrogated pSTAT1 and CXCL10 levels (Figures 3C and 3D). Together, these results are consistent with the role of PARP7 negatively regulating PRR signaling in cancer cells.

To test whether the effect of RBN-2397 on antitumor immunity depends on type I IFN signaling *in vivo*, we administered vehicle or RBN-2397 (100 mg/kg) CT26 to WT or PRR pathway gene KO tumor-bearing mice. We found that ablation of tumor TBK1 or STING nearly eliminated the response to RBN-2397 (Figure 3E), suggesting that tumor-derived IFN is the source of the immune activation and is crucial for the RBN-2397-mediated antitumor response. In contrast, antitumor activity of RBN-2397 was initially attenuated in IFNAR1 KO tumors, but a subset of tumors began to respond after day 12. Administration of a blocking anti-IFNAR1 antibody in this system to block non-tumor IFNAR responses completely prevented tumor regression. This delayed response seen in IFNAR1 KO tumors, which was sensitive to inhibition by anti-IFNAR1 antibody, suggests that the onset of antitumor immu-

nity is dependent on the effects of tumor-derived IFN on immune cells (Figure 3E). Further supporting this interpretation, administration of the anti-IFNAR1 antibody to mice bearing WT tumors phenocopied the results of the IFNAR1 KO plus anti-IFNAR antibody (Figure 3E). Based on these findings, it appears that tumor-produced type I IFN, induced through inhibition of PARP7 by RBN-2397, plays a major role in the development of durable antitumor immunity in this system.

RBN-2397 displays cell-autonomous effects in human cancer models

To investigate the cell-autonomous effects of PARP7 inhibition, we screened a set of three PARP7 inhibitors (supplemental information) across 125 human cell lines derived from multiple cancer types and identified a subset of cancer cell lines exhibiting dependency on PARP7 for proliferation (Figure 5A and Table S3).

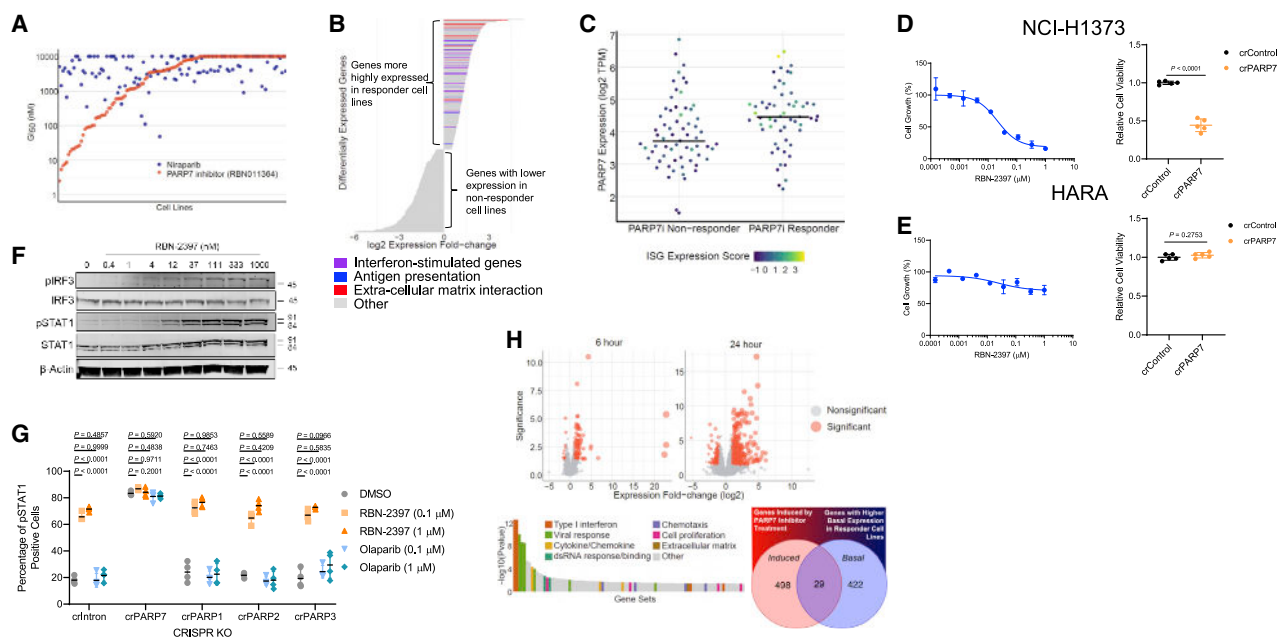


Figure 5. RBN-2397 cell-autonomous effects in human cancer cell lines

(A) Representative GI_{50} data for RBN011364 (PARP7 inhibitor) and niraparib (see Table S3 for responder cell lines and supplemental information for PARP7 inhibitors).

(B) Differentially expressed genes at baseline between responder and non-responder cell lines.

(C) PARP7 expression levels by PARP7 inhibition response groups. Each point represents a cell line screened with PARP7 inhibitors, the color indicating the ISG expression score of the cell line.

(D) Effects of RBN-2397 on proliferation of NCI-H1373 cells (left; representative data shown as mean \pm SD, $n = 3$, experiment repeated 46 times) or acute PARP7 knockout by CRISPR/Cas9 on proliferation of NCI-H1373 cells (right; representative data shown as mean \pm SD, $n = 5$, experiment repeated three times, p value determined by a two-tailed Student's t test).

(E) Effects of RBN-2397 on proliferation of HARA cells (left; representative data shown as mean \pm SD, $n = 3$, experiment repeated three times) or acute PARP7 knockout by CRISPR/Cas9 on proliferation of HARA cells (right; representative data shown as mean \pm SD, $n = 5$, experiment repeated three times, p value determined by a two-tailed Student's t test).

(F) Effects of RBN-2397 on type I IFN signaling in NCI-H1373 cells measured by the induction of IRF3 or STAT1 phosphorylation. Representative data shown from a single experiment, experiment repeated twice.

(G) Effects of PARPs 1, 2, 3, or 7 acute KO in NCI-H1373 cells by CRISPR/Cas9 on RBN-2397-induced pSTAT1 determined by immunofluorescence. Representative data shown as mean \pm SD, $n = 4$, experiment repeated twice, p value determined by one-way ANOVA.

(H) NCI-H1373 cells were treated with RBN-2397 and lysates were subjected to RNA sequencing. Volcano plot shows transcriptional changes (red: significant; gray: not significant) by RBN-2397 in NCI-H1373 cells (top). GSEA of upregulated genes (bottom left) and Venn diagram (bottom right) depicting overlap of gene expression changes. Significant gene expression changes defined by the false discovery rate (FDR) < 0.05 and fold change > 2 .

We found remarkably differential responses between the PARP7 inhibitor (RBN011364) and niraparib, with niraparib showing 80-fold more potent activity in the BRCA mutant MDA-MB-436 cell line (RBN011364 GI_{50} : 4,000 nM and niraparib GI_{50} : 50 nM; Figure 5A and Table S3), suggesting that PARP7 inhibitors show selective pharmacology in a subset of cancers. Responder cell lines ($n = 59$; Table S3) were significantly enriched for high expression of genes involved in type I IFN response and antigen presentation (Figure 5B). Further analysis showed that both PARP7 expression and the published ISG score (Liu et al., 2019) were significantly higher among responder cell lines (Figure 5C). We used the CRISPR/Cas9 system to ablate PARP7 in sensitive (NCI-H1373) and insensitive (HARA) lung cancer cells and found that acute genetic KO of PARP7 phenocopied the cellular activity of PARP7 catalytic inhibition via RBN-2397 in both cell lines (Figures 5D and 5E). RBN-2397 treatment of cells in which PARP7 was simultaneously being acutely knocked out resulted in resistance to catalytic inhibition in sensitive NCI-

H1373 but not insensitive HARA cells, demonstrating on-target antiproliferative activity of RBN-2397 (Figures S6A and S6B). Furthermore, the inactive analog, RBN250036, as well as two PARP1 inhibitors, niraparib and olaparib, showed little to no activity in the NCI-H1373 cell line (GI_{50} s $> 1,000$ nM; Figure S6C). We further characterized the phenotypic effects of PARP7 inhibition in NCI-H1373 and found that RBN-2397 significantly increases the number of cells in the G_0/G_1 phase of the cell cycle, indicative of a cell-cycle arrest (Figure S6D). This arrest in NCI-H1373 cells appeared to be due to induction of senescence, as shown by β -galactosidase staining (Figure S6D) and increased mRNA expression of several SASP (senescence-associated secretory phenotype) genes (Figure S6D).

We next evaluated the effects of PARP7 inhibition on type I IFN signaling in the human NCI-H1373 cell line model and found that RBN-2397 induced a concentration-dependent increase in IRF3 and STAT1 phosphorylation (Figures 5F and S7A) and CXCL10 (Figure S7B) compared with the inactive analog, RBN250036.

Acute KO of PARP7 in NCI-H1373 cells showed the same enhancement of pIRF3 and pSTAT1 (Figures 5G and S7C). Simultaneous KO of PARP7 prevented any additional increase of IRF3 or STAT1 phosphorylation by RBN-2397; however, KO of PARPs 1, 2, or 3 had no effect on the induction of type I IFN signaling by RBN-2397, further supporting the on-target activity of RBN-2397 for PARP7 in both mouse and human cell lines (Figures 5G and S7C). The PARP1 inhibitor olaparib showed no effect on pSTAT1 or pIRF3 (Figures 5G and S7C) or CXCL10 (Figure S7B). We also observed no effects on pIRF3 and pSTAT1 in two normal cell lines, BEAS-2B (lung epithelial) and MRC-5 (fibroblast) treated with RBN-2397 (Figure S7D). Similar to the results found with the mouse CT26 cell line (described in Figure 3), RBN-2397 restored type I IFN signaling through TBK1 and JAK in NCI-H1373 cells (Figure S7E). Additionally, we found that acute KO of cGAS or STING by CRISPR/Cas9 prevented induction of both pIRF3 and pSTAT1 by RBN-2397 in NCI-H1373 cells, but KO of RIG-I did not affect downstream signaling (Figure S7F), suggesting that the DNA-sensing pathway is essential for the effects of RBN-2397 on type I IFN signaling in NCI-H1373 cells.

We next investigated transcriptional changes after RBN-2397 treatment in two PARP7 inhibitor-sensitive cell lines, NCI-H1373 and NCI-H647, by RNA sequencing. The majority of gene expression changes were transcriptional increases at the 24-h time point (Figures 5H and S8; Table S2). Based on gene set enrichment analysis (GSEA), upregulated genes from PARP7 inhibition were significantly enriched in type I IFN signaling and viral response genes in both cell lines (Figures 5H and S8). We also observed that many ISGs whose baseline expression predicted *in vitro* sensitivity to PARP7 inhibition (Figure 5B) were further transcriptionally increased by RBN-2397 (Figures 5H and S8), suggesting that a primed state of IFN signaling in sensitive cells is further enhanced by PARP7 inhibition.

Type I IFN pathway genes confer resistance and sensitivity to RBN-2397 for proliferation

To further explore how RBN-2397 inhibits NCI-H1373 cell proliferation, we performed unbiased genetic screens using whole-genome CRISPRi and CRISPRa libraries (le Sage et al., 2017; Jost and Weissman, 2018). Comparison of CRISPRi and CRISPRa phenotype scores highlighted genes with opposing functionality upon RBN-2397 treatment (Figure 6A and Table S4). GSEA analysis showed that genes involved in innate immune response, regulation of chemokine production, and Toll-like receptor signaling resulted in resistance to RBN-2397 when silenced (CRISPRi) or sensitivity when activated (CRISPRa; Figure 6B). A custom CRISPR array comprising 234 genes involved in innate immunity, helicase activity, and cytosolic RNA/DNA sensing was used to validate the findings of the CRISPRi/a screen and to further investigate the role of PARP7 in regulating the type I IFN response in cancer cells. Consistent with results from the CRISPRi/a screen, genetic KO of key components of type I IFN signaling, such as cGAS (MB21D1) and IFNAR1, conferred resistance to RBN-2397 (Figures 6C and S9; Table S5). These data indicate that PARP7 suppresses the type I IFN response in NCI-H1373 cells and that inhibiting PARP7 with RBN-2397 reactivates the pathway, leading to inhibition of cancer cell proliferation.

To identify PARP7 substrates in cancer cells, we quantified ADP-ribosylated proteins from cells with differential PARP7 ac-

tivity (either PARP7-inhibitor treated or with PARP7 overexpression) via an enrichment-mass spectrometry approach (Lu et al., 2019). Proteins found to be differentially ADP-ribosylated were considered as PARP7 substrate candidates (Table S6). These putative PARP7 substrates were then compared with the hits from the CRISPR screens described above. Concordance of the phenotype between both CRISPR screens occurred in 18 substrates (Figure 6D). Among the four resistance hits, we identified PARP7 and AHR as substrates. AHR transcriptionally regulates PARP7 and was previously validated as a PARP7 substrate (Lu et al., 2019; Gomez et al., 2018). Several PARP7 substrates were regulators of the type I IFN response. For example, ADAR, an enzyme that negatively regulates cytosolic RNA sensing (Ishizuka et al., 2019; Mannion et al., 2014), is a PARP7 substrate, and KO of its gene confers sensitivity to RBN-2397 (Figures 6D and S9). These data demonstrate that PARP7 negatively regulates type I IFN signaling downstream of nucleic acids at multiple steps in the pathway.

Antitumor activity of RBN-2397 in human xenografts

We next investigated the relationship between RBN-2397 antiproliferative activity and induction of type I IFN response in a panel of cancer cell lines. We found that the majority of cell lines that are sensitive to RBN-2397 antiproliferative activity also show induction of ISGs (Figures 7A, S10A, and S10B). Both RBN-2397 antiproliferative activity and induction of ISGs by RBN-2397 were independent of the levels of cGAMP or cytosolic DNA across the panel of cell lines (Figures S10C and S10D). When grown as xenografts in CB17 SCID mice, QD dosing of RBN-2397 led to antitumor activity (Figure S10E) in all cell models that showed an induction of ISGs *in vitro* (Figures 7A and S10B). We also observed modest antitumor activity (53%–78%) in four lung cancer patient-derived xenograft models, further supporting the tumor-intrinsic activity of RBN-2397 (Figure S10F). RBN-2397 did not show any antitumor activity in the HARA xenograft model (Figure S10E) that was also a non-responder *in vitro* (Figure 5E). Taken together, reactivation of tumor-intrinsic type I IFN signaling is a major determinant of the antitumor activity of RBN-2397 *in vivo*.

While RBN-2397 slowed tumor growth (TGI: 49%–67%) in most xenograft models, we observed complete tumor regression in the NCI-H1373 xenograft with either once- or twice-daily dosing of 500 mg/kg RBN-2397. Tumor regressions were durable for at least 11 days after RBN-2397 dosing was stopped, and tumors that regrew to either the initial starting tumor size (approximately 122 mm³) or to larger more established tumors (approximately 530 mm³) remained sensitive to RBN-2397 upon retreatment (Figure 7B). We next examined the antitumor effects of once-daily orally administered RBN-2397 in CB17 SCID mice with subcutaneous NCI-H1373 xenograft tumors over a dose range. We observed a dose-dependent effect of RBN-2397 on tumor growth, with tumor regressions at dose levels ≥ 30 mg/kg (Figure 7C). Increased antitumor activity was associated with increased RBN-2397 exposure as measured by plasma levels over time (Figure S11A). In addition, all three intermittent dosing schedules tested at 300 mg/kg resulted in tumor regression (Figure S11B). We observed that RBN-2397 significantly decreased ADP ribosylation at 24 h and increased human tumor cell-expressed *IFN- β* , *MX1*, and *IFIT1* mRNA

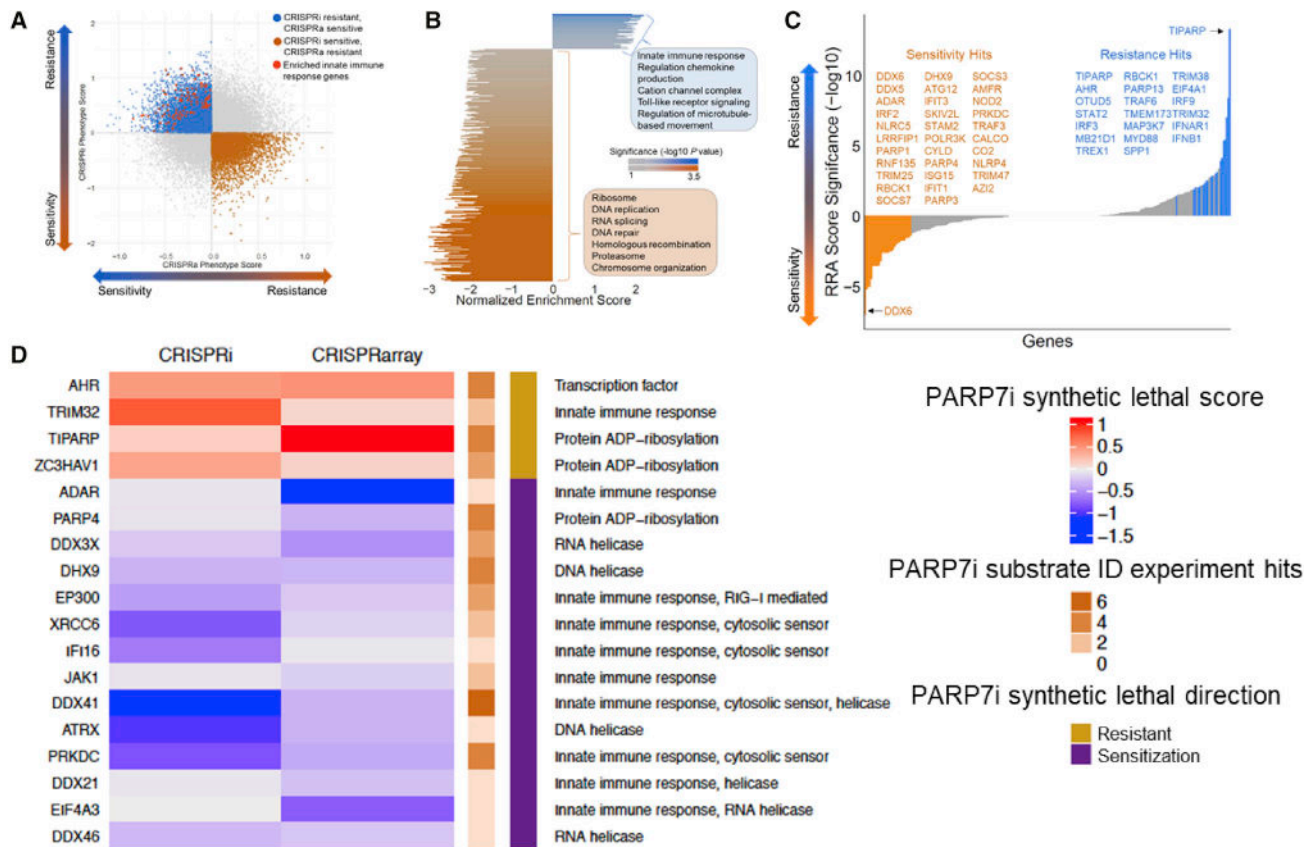


Figure 6. Genes involved in type I IFN signaling confer resistance and sensitivity to RBN-2397

(A) Biplot of CRISPRi/a gene scores in RBN-2397 treated NCI-H1373 cells. Genes with opposing CRISPRi/a effects are colored blue and orange. (B) Waterfall plot of significantly enriched gene sets using CRISPRi-resistant/CRISPRa-sensitive (blue) and CRISPRi-sensitive/CRISPRa-resistant (orange) scores. (C) Waterfall plot of gene hits identified in CRISPR knockout array screen with RBN-2397 ranked by robust rank aggregation (RRA) score. Genes are listed to match bars that have RRA FDR < 0.05 and consistent fold changes in the corresponding direction. (D) Overlay of CRISPRi phenotype scores, CRISPR KO array (maximum log fold-change values), and substrate ID datasets. Substrate ID experimental hits are defined as observed reduction in ADP ribosylation with PARP7 inhibitor (RBN011364, see [supplemental information](#)) treatment compared with vehicle treatment.

levels, and both *CXCL10* mRNA and protein levels, in an exposure-dependent manner compared with vehicle control (Figures 7D, S11C, and S11D). We also observed an induction of STAT1 phosphorylation in the tumor by RBN-2397 (Figure S11E).

While CB17 SCID mice lack cells of the adaptive immune system, they still have innate immune cells such as NK cells and macrophages that can be activated by type I IFNs (Zitvogel et al., 2015). Using CB17 SCID mice treated with anti-asialoGM1 antibodies to deplete NK cells, we observed that RBN-2397 antitumor activity is independent of NK cells in the NCI-H1373 model (Figures S12A and S12B). Additional assessment of RBN-2397 antitumor activity in SCID beige mice that lack functional NK cells (Roder and Duwe, 1979) showed similar results (Figure S12C). These data support the notion that RBN-2397 antitumor activity in this model is mediated by tumor-intrinsic activity and not by activation of NK cells in this model. We next evaluated the role of type I IFN signaling on the tumor-intrinsic effects of RBN-2397 in NCI-H1373 xenografts using CRISPR/Cas9 to knock out TBK1. Although KO of TBK1 only resulted in partial resistance to RBN-2397, it completely prevented tumor regression (Figure 7E). These data suggest that TBK1/type I IFN signaling plays a partial

role in controlling tumor growth in an immunodeficient model and that other TBK1-independent pathways may be involved.

DISCUSSION

A growing body of literature suggests that one of the consequences of genetic instability in cancer is the presence of aberrant nucleic acids in the cytosol (Paludan et al., 2019; Hatch et al., 2013; Harding et al., 2017; Mackenzie et al., 2017; Gluck et al., 2017). Typically, this triggers damage-associated molecular PRR signaling, for instance through the cGAS/STING or RIG-I systems, and the type I IFN response (Ivashkiv and Donlin, 2014; Barber, 2015; Ishikawa and Barber, 2008; Ahn et al., 2014; Hartlova et al., 2015). Activation of this pathway at low levels may promote tumor growth, but strong activation is thought to promote growth arrest and/or elimination by the immune system (Cheon et al., 2014). Cancer cells may be under selective pressure to control tumoral IFN signaling. For instance, the RNA-editing enzyme ADAR has been suggested to render nucleic acids invisible to PRRs and may be upregulated in cancer cells to suppress the type I IFN response (Ishizuka et al., 2019; Liu et al.,

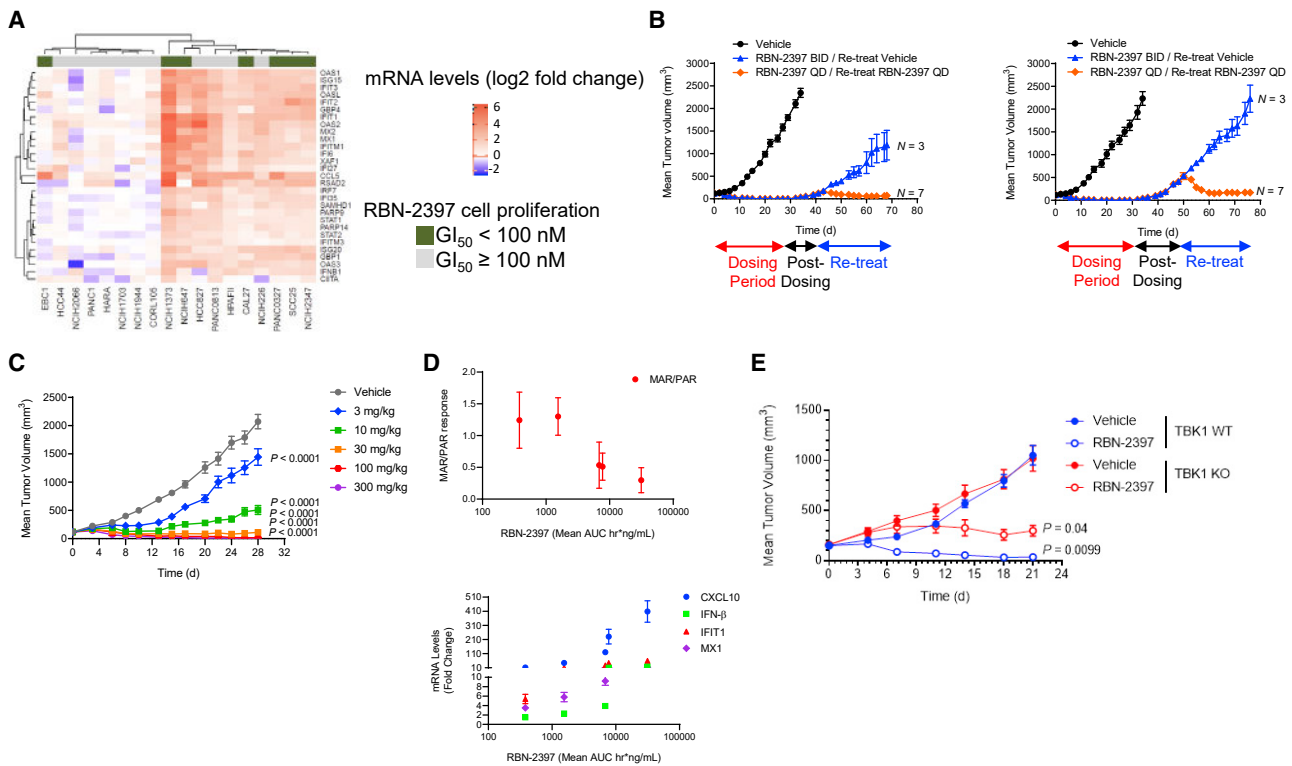


Figure 7. RBN-2397 causes complete regression in human NCI-H1373 lung cancer xenografts

(A) Heatmap showing relationship between sensitivity to RBN-2397 for proliferation and ISG expression determined by NanoString (single experiment) across a panel of cancer cell lines.

(B) Antitumor activity of 500 mg/kg RBN-2397 in CB17 SCID subcutaneous tumor model with NCI-H1373 cells. Tumor-bearing mice (mean tumor size of 118 mm³, n = 10) were dosed orally with either vehicle or RBN-2397 at the indicated dose and schedule. Mice were monitored for tumor regrowth and were retreated with either vehicle (blue line) or RBN-2397 (orange line) when tumor volumes reached either 122 mm³ (left panel) or 530 mm³ (right panel). Mean tumor volume and SEM are plotted.

(C) Antitumor activity of RBN-2397 over a dose range (QD × 28 days) in CB17 SCID subcutaneous tumor model with NCI-H1373 cells. Treatment initiated with mean tumor size of 118 mm³. Mean tumor volume and SEM are plotted, n = 10. p value determined by two-way ANOVA with multiple comparisons on day 28. QD, once daily.

(D) Exposure-dependent decrease of tumoral monoADP ribosylation (MAR, top) and increase of *IFN-β*, *CXCL10*, *IFIT1*, and *MX1* mRNAs (bottom) in NCI-H1373 tumor-bearing mice dosed with RBN-2397. Data are shown as mean ± SD, n = 5, experiment repeated twice with similar results.

(E) Antitumor activity of 300 mg/kg RBN-2397 (QD × 21 days) in CB17 SCID subcutaneous tumor model with wild-type (WT) and TBK1 KO NCI-H1373 cells. Treatment initiated with mean tumor size of 150 or 159 mm³ for WT and TBK1 KO, respectively. Mean tumor volume and SEM are plotted, n = 10. p value determined by a two-tailed Student's t test on day 21. QD, once daily.

2019; Gannon et al., 2018). Here, we show that some cancer cells use PARP7 to reduce the type I IFN response to nucleic acids. We discovered PARP7 to be a connection between immune-regulatory AHR signaling and the type I IFN pathway in cancer. We hypothesize that increased PARP7 expression due to gene amplification or transcriptional activation by AHR leads to chronic suppression of tumor IFN signaling. This allows the cancer cell to grow and avoid immunosurveillance despite the presence of cytosolic DNA or/and aberrant RNA.

Agents that engage innate immunity pathways, such as STING agonists, have been proposed as cancer treatment strategies and have recently entered clinical testing (Galon and Bruni, 2019; Vanpouille-Box et al., 2019; Flood et al., 2019). STING agonists activate innate immunity by targeting immune cells within the tumor microenvironment to mediate an adaptive immune response but cannot trigger productive IFN signaling and antiproliferative activity in tumor cells themselves (Flood,

2017). Because their effects rest on activation of cells of the immune system, they lack specificity for tumors and may trigger whole-body inflammation (Ramanjulu et al., 2018). PARP1 inhibitors, originally approved to target DNA repair defects in cancer, have been recently shown to increase cytosolic DNA and cGAMP levels leading to cGAS-STING activation in cells with defects in their DNA repair machinery. In this context, PARP1 inhibitors have been shown to trigger antitumor immune responses in preclinical BRCA-deficient mouse models (Pantelidou et al., 2019; Shen et al., 2019; Ding et al., 2018). In contrast, we have demonstrated that inhibition of PARP7 by the small-molecule inhibitor RBN-2397 restores type I IFN signaling in tumor cells by releasing a brake on aberrant nucleic acid sensing, thus enhancing innate immunity within the tumor environment rather than systemically. In addition, these tumor-specific responses are not limited to cancers with DNA repair defects.

The on-target inhibition of PARP7 by RBN-2397 causes both direct inhibition of cell proliferation and activation of signaling to the immune system. Oral dosing of RBN-2397 results in durable, complete tumor regression in a human lung cancer xenograft and regression followed by tumor-specific adaptive immune memory in a mouse syngeneic model, which can be amplified in combination with anti-PD-1 checkpoint inhibition. Interestingly, stable KO of PARP7 in CT26 cells did not phenocopy the antitumor effects observed with RBN-2397. Stable KO of PARP7 results in only a modest increase of type I signaling (Figures 1H and 1I), so it is possible that the cells have adapted to suppress chronic type I signaling. In contrast, acute KO of PARP7 results in a similar type I IFN response compared with RBN-2397 in NCI-H1373 cells (Figures 5G and 5C); therefore, it is unclear whether a conditional KO would be more comparable with a small molecule *in vivo*. Another intriguing possibility is that RBN-2397 is not only preventing the catalytic activity of PARP7 but is also working by trapping PARP7 on a substrate affecting protein function.

Our *in vivo* data in human and mouse cancer models suggest that antitumor activity can be achieved without a fully functioning immune system; however, to achieve maximal and durable regressions tumor cell-induced immune activation is necessary. Our data support that PARP7 but not PARPs 1, 2, 3, or 12 is indispensable for the immunomodulatory activity of RBN-2397. We did observe enhanced antitumor immunity with PARP2, PARP3, and PARP12 KO CT26 cells and sensitization to RBN-2397 with PARP1 and PARP3 KO NCI-H1373 cells, suggesting the possibility to combine with agents that target other PARPs. Our mechanistic studies indicate that active signaling through PRRs and IFNAR1 in tumor cells is required for the antitumor activity of RBN-2397, and that PARP7-mediated ADP ribosylation regulates the activity of multiple signaling nodes of this innate immunity pathway. This includes inputs from both DNA and RNA arms of the pathways, with the RNA arm evidenced by ADAR being both a PARP7 substrate and sensitivity determinant. Cancer cell lines that have increased expression of ISGs at baseline tend to be more responsive to PARP7 inhibition, and RBN-2397 treatment increases gene expression of several of the same ISGs further. This suggests that certain cancers exhibit constitutive, low-level IFN signaling that is negatively regulated by PARP7 to allow cancer cell survival and immune evasion. PARP7 inhibition releases that negative regulation, leading to cancer cell arrest and tumor targeting by the immune system. The concept of cancers with high-baseline ISG signaling has recently been introduced by analyzing data from The Cancer Genome Atlas (Liu et al., 2019) and represents a potential patient enrichment strategy for RBN-2397 testing in clinical trials. Together, our preclinical data demonstrate the PARP7 inhibitor RBN-2397 as a cancer treatment, and a phase 1 clinical trial is under way (Falchook et al., 2021; NCT04053673) (clinicaltrials.gov, 2019).

STAR★METHODS

Detailed methods are provided in the online version of this paper and include the following:

- KEY RESOURCES TABLE
- RESOURCE AVAILABILITY

- Lead contact
- Materials availability
- Data and code availability

● EXPERIMENTAL MODEL AND SUBJECT DETAILS

- Mouse strains
- Cell lines

● METHOD DETAILS

- TCGA and dependency map analysis
- Surface plasmon resonance (SPR)
- Biochemical PARP inhibition assays
- MAR/PAR in-cell western (ICW) assay
- Active site probe displacement NanoBRET assay
- RNA detection assay for PARP7-mediated *CYP1B1* RNA regulation
- Cell proliferation
- Cancer cell line screen
- Cell cycle and senescence assays
- PARP7 overexpression
- 2'3'-cGAMP ELISA
- Cytosolic DNA detection
- Transfection of PRR ligands
- nanoString analysis
- RNA sequencing
- Western blotting
- Immunofluorescence staining and imaging
- CRISPRi/a screen
- CRISPR gene KO
- CRISPR arrayed screening
- Generation of CRISPR KO CT26 cells
- Substrate ID by mass spectrometry
- *In vivo* studies
- PDX studies
- Tumor re-challenge
- *In vivo* immune depletion
- Immunophenotyping
- Quantitative PCR (QPCR)
- CXCL10 ELISA
- *Ex vivo* T cell response using IFN- γ ELISPOT

● QUANTIFICATION AND STATISTICAL ANALYSIS

SUPPLEMENTAL INFORMATION

Supplemental information can be found online at <https://doi.org/10.1016/j.ccell.2021.06.018>.

ACKNOWLEDGMENTS

We thank Sudha Parasuraman, Tad Stewart, Kristen McEachern, Patrick Flynn, Lee Kraus, Paul Chang, and Larry Lasky for their useful comments. We thank Ping Wei for protein production efforts. We thank Chang Liu and Bryan Dorsey for their computational support. The authors thank all current and past members of Ribon Therapeutics for their support and contributions as well as the teams who have helped to support this work at ChemPartner, Pharmaron, Covance, Canopy Biosciences, Horizon Discovery, and intoDNA.

AUTHOR CONTRIBUTIONS

J.M.G. and H.K. contributed to writing the manuscript with contributions from all authors. R.P.A. conducted the bioinformatics analyses. C.R.M., T.J.W., D.J.B., Y.R., K.G.K.-B., Z.A.V., K.K., A.Z.L., W.D.C., E.B., J.-R. Mo, J.S., J.R. Molina, E.M., A.S.A.M., and S.P.N. performed the *in vitro* studies and analyzed the *in vitro* data. K.K.S. solved the X-ray structure and expressed

and purified the PARP7 protein. M.M.V. designed and executed compound synthesis. B.G. designed and performed the CRISPR library preparation and R.P.A., J.M.G., and M.N. contributed to the analysis. K.K., J.M.G., and L.U. designed, executed, and analyzed the *in vivo* studies. J.M.G., H.K., M.N., J.R. Molina, P.E.R., T.J.M., K.W.K., T.J.W., and V.M.R. provided guidance on experimental design and analyses.

DECLARATION OF INTERESTS

J.M.G., M.M.V., R.P.A., K.K., K.G.K.-B., B.G., A.Z.L., J.R. Molina, E.M., K.K.S., T.J.W., D.J.B., C.R.M., Y.R., M.N., Z.A.V., S.P.N., E.B., J.-R. Mo, W.D.C., A.S.A.M., J.S., L.U., K.W.K., V.M.R., and H.K. are all employees and shareholders of Ribon Therapeutics at the time of data collection. P.E.R. served as a consultant to Ribon Therapeutics, and T.J.M. is a founder and shareholder in Ribon Therapeutics. M.M.V., K.K.S., and K.W.K. are inventors on US Patent Nos. 10550105, 10870641, and 11014913, which are related to RBN-2397 and assigned to Ribon Therapeutics.

Received: August 21, 2020

Revised: May 25, 2021

Accepted: June 25, 2021

Published: July 22, 2021

REFERENCES

clinicaltrials.gov (2019). RBN-2397, an oral PARP7 inhibitor, in Patients with Solid Tumors, FIH, MAD Study. <https://clinicaltrials.gov/ct2/show/NCT04053673>.

Ahn, J., Xia, T., Konno, H., Konno, K., Ruiz, P., and Barber, G.N. (2014). Inflammation-driven carcinogenesis is mediated through STING. *Nat. Commun.* **5**, 5166.

Barber, G.N. (2015). STING: infection, inflammation and cancer. *Nat. Rev. Immunol.* **15**, 760–770.

Borden, E.C. (2019). Interferons alpha and beta in cancer: therapeutic opportunities from new insights. *Nat. Rev. Drug Discov.* **18**, 219–234.

Cheon, H., Borden, E.C., and Stark, G.R. (2014). Interferons and their stimulated genes in the tumor microenvironment. *Semin. Oncol.* **41**, 156–173.

Clark, K., Plater, L., Pegg, M., and Cohen, P. (2009). Use of the pharmacological inhibitor BX795 to study the regulation and physiological roles of TBK1 and IkkappaB kinase epsilon: a distinct upstream kinase mediates Ser-172 phosphorylation and activation. *J. Biol. Chem.* **284**, 14136–14146.

Cohen, M.S., and Chang, P. (2018). Insights into the biogenesis, function, and regulation of ADP-ribosylation. *Nat. Chem. Biol.* **14**, 236–243.

Corrales, L., Glickman, L.H., McWhirter, S.M., Kanne, D.B., Sivick, K.E., Katibah, G.E., Woo, S.R., Lemmens, E., Banda, T., Leong, J.J., et al. (2015). Direct activation of STING in the tumor microenvironment leads to potent and systemic tumor regression and immunity. *Cell Rep.* **11**, 1018–1030.

Cross, B.C.S., Lawo, S., Archer, C.R., Hunt, J.R., Yarker, J.L., Riccombeni, A., Little, A.S., McCarthy, N.J., and Moore, J.D. (2016). Increasing the performance of pooled CRISPR-Cas9 drop-out screening. *Sci. Rep.* **6**, 31782. <https://doi.org/10.1038/srep31782>.

Dempster, J.M., Rossen, J., Kazachkova, M., Pan, J., Kugener, G., Root, D.E., and Tsherniak, A. (2019). Extracting biological insights from the project Achilles genome-scale CRISPR screens in cancer cell lines. *bioRxiv*. <https://doi.org/10.1101/720243>.

Ding, L., Kim, H.J., Wang, Q., Kearns, M., Jiang, T., Ohlson, C.E., Li, B.B., Xie, S., Liu, J.F., Stover, E.H., et al. (2018). PARP inhibition elicits STING-dependent antitumor immunity in *brca1*-deficient ovarian cancer. *Cell Rep.* **25**, 2972–2980.e2975.

Falchook, G.S., Patel, M.R., Yap, T.Y., McEachern, K., Kuplast-Barr, K., Utley, L., Cleary, L., Manyak, E., Bozon, V., Parasuraman, S., et al. (2021). A first-in-human phase 1 study of a novel PARP7 inhibitor RBN-2397 in patients with advanced solid tumors. *J. Clin. Oncol.* **39**, abstr. 3000. https://doi.org/10.1200/JCO.2021.39.15_suppl.3000.

Flood, B. (2017). Tumor cell-intrinsic STING signaling and regulation of IFN- β gene expression. Paper presented at: Society for Immunotherapy of Cancer 32nd Annual Meeting (SITC 2017).

Flood, B.A., Higgs, E.F., Li, S., Luke, J.J., and Gajewski, T.F. (2019). STING pathway agonism as a cancer therapeutic. *Immunol. Rev.* **290**, 24–38.

Galon, J., and Bruni, D. (2019). Approaches to treat immune hot, altered and cold tumours with combination immunotherapies. *Nat. Rev. Drug Discov.* **18**, 197–218.

Gannon, H.S., Zou, T., Kiessling, M.K., Gao, G.F., Cai, D., Choi, P.S., Ivan, A.P., Buchumenski, I., Berger, A.C., Goldstein, J.T., et al. (2018). Identification of ADAR1 adenosine deaminase dependency in a subset of cancer cells. *Commun* **9**, 5450.

Gluck, S., Guey, B., Nat Gulen, M.F., Wolter, K., Kang, T.W., Schmacke, N.A., Bridgeman, A., Rehwinkel, J., Zender, L., and Ablasser, A. (2017). Innate immune sensing of cytosolic chromatin fragments through cGAS promotes senescence. *Nat. Cell Biol.* **19**, 1061–1070.

Gomez, A., Bindsboll, C., Satheesh, S.V., Grimaldi, G., Hutin, D., MacPherson, L., Ahmed, S., Tamblyn, L., Cho, T., Nebb, H.I., et al. (2018). Characterization of TCDD-inducible poly-ADP-ribose polymerase (TIPARP/ARTD14) catalytic activity. *Biochem. J.* **475**, 3827–3846.

Gu, Z., Eils, R., and Schlesner, M. (2016). Complex heatmaps reveal patterns and correlations in multidimensional genomic data. *Bioinformatics* **32**, 2847–2849.

Haag, S.M., Gulen, M.F., Reymond, L., Gibelin, A., Abrami, L., Decout, A., Heymann, M., van der Goot, F.G., Turcatti, G., Behrendt, R., et al. (2018). Targeting STING with covalent small-molecule inhibitors. *Nature* **559**, 269–273.

Harding, S.M., Benci, J.L., Irianto, J., Discher, D.E., Minn, A.J., and Greenberg, R.A. (2017). Mitotic progression following DNA damage enables pattern recognition within micronuclei. *Nature* **548**, 466–470.

Hartlova, A., Erttmann, S.F., Raffi, F.A., Schmalz, A.M., Resch, U., Anugula, S., Lienenklaus, S., Nilsson, L.M., Kroger, A., Nilsson, J.A., et al. (2015). DNA damage primes the type I interferon system via the cytosolic DNA sensor STING to promote anti-microbial innate immunity. *Immunity* **42**, 332–343.

Hatch, E.M., Fischer, A.H., Deerinck, T.J., and Hetzer, M.W. (2013). Catastrophic nuclear envelope collapse in cancer cell micronuclei. *Cell* **154**, 47–60.

Huang, A.Y., Gulden, P.H., Woods, A.S., Thomas, M.C., Tong, C.D., Wang, W., Engelhard, V.H., Pasternack, G., Cotter, R., Hunt, D., et al. (1996). The immunodominant major histocompatibility complex class I-restricted antigen of a murine colon tumor derives from an endogenous retroviral gene product. *Proc. Natl. Acad. Sci. U S A* **93**, 9730–9735.

Ishikawa, H., and Barber, G.N. (2008). STING is an endoplasmic reticulum adaptor that facilitates innate immune signalling. *Nature* **455**, 674–678.

Ishizuka, J.J., Manguso, R.T., Cheruiyot, C.K., Bi, K., Panda, A., Iracheta-Vellve, A., Miller, B.C., Du, P.P., Yates, K.B., Dubrot, J., et al. (2019). Loss of ADAR1 in tumours overcomes resistance to immune checkpoint blockade. *Nature* **565**, 43–48.

Ivashkiv, L.B., and Donlin, L.T. (2014). Regulation of type I interferon responses. *Nat. Rev. Immunol.* **14**, 36–49.

Jones, P., Wilcoxon, K., Rowley, M., and Toniatti, C. (2015). Niraparib: a poly(ADP-ribose) polymerase (PARP) inhibitor for the treatment of tumors with defective homologous recombination. *J. Med. Chem.* **58**, 3302–3314.

Jost, M., and Weissman, J.S. (2018). CRISPR approaches to small molecule target identification. *ACS Chem. Biol.* **13**, 366–375.

Kolde, R., Laur, S., Adler, P., and Vilo, J. (2012). Robust rank aggregation for gene list integration and meta-analysis. *Bioinformatics* **4**, 573–580.

Kordon, M.M., Zarebski, M., Solarczyk, K., Ma, H., Pederson, T., and Dobrucki, J.W. (2020). STRIDE—a fluorescence method for direct, specific *in situ* detection of individual single- or double-strand DNA breaks in fixed cells. *Nucleic Acids Res.* **48**, e14.

Li, W., Xu, H., Cong, L., Love, M.I., Zhang, F., Irizzary, R.A., Liu, J.S., Brown, M., and Liu, X.S. (2014). MAGeCK enables robust identification of essential

- genes from genome-scale CRISPR/Cas9 knockout screens. *Genome Biol.* **15**, 554.
- Liu, H., Golji, J., Brodeur, L.K., Chung, F.S., Chen, J.T., deBeaumont, R.S., Bullock, C.P., Jones, M.D., Kerr, G., Li, L., et al. (2019). Tumor-derived IFN triggers chronic pathway agonism and sensitivity to ADAR loss. *Nat. Med.* **25**, 95–102.
- Love, M.I., Huber, W., and Anders, S. (2014). Moderated estimation of fold change and dispersion for RNA-seq data with DESeq2. *Genome Biol.* **15**, 550.
- Lu, A.Z., Abo, R., Ren, Y., Gui, B., Mo, J.R., Blackwell, D., Wigle, T., Keilhack, H., and Niepel, M. (2019). Enabling drug discovery for the PARP protein family through the detection of mono-ADP-ribosylation. *Biochem. Pharmacol.* **167**, 97–106.
- Luo, J., Solimini, N.L., and Elledge, S.J. (2009). Principles of cancer therapy: oncogene and non-oncogene addiction. *Cell* **136**, 823–837.
- Mackenzie, K.J., Carroll, P., Martin, C.A., Murina, O., Fluteau, A., Simpson, D.J., Olova, N., Sutcliffe, H., Rainger, J.K., Leitch, A., et al. (2017). cGAS surveillance of micronuclei links genome instability to innate immunity. *Nature* **548**, 461–465.
- MacPherson, L., Tamblin, L., Rajendra, S., Bralha, F., McPherson, J.P., and Matthews, J. (2013). 2,3,7,8-Tetrachlorodibenzo-p-dioxin poly(ADP-ribose) polymerase (TIPARP, ARTD14) is a mono-ADP-ribosyltransferase and repressor of aryl hydrocarbon receptor transactivation. *Nucleic Acids Res.* **41**, 1604–1621.
- MacPherson, L., Ahmed, S., Tamblin, L., Krutmann, J., Forster, I., Weighardt, H., and Matthews, J. (2014). Aryl hydrocarbon receptor repressor and TIPARP (ARTD14) use similar, but also distinct mechanisms to repress aryl hydrocarbon receptor signaling. *Int. J. Mol. Sci.* **15**, 7939–7957.
- Majoros, A., Platanitis, E., Kernbauer-Holz, E., Rosebrock, F., Muller, M., and Decker, T. (2017). Canonical and non-canonical aspects of JAK-STAT signaling: lessons from interferons for cytokine responses. *Front. Immunol.* **8**, 29.
- Mannion, N.M., Greenwood, S.M., Young, R., Cox, S., Brindle, J., Read, D., Nellaker, C., Vesely, C., Ponting, C.P., McLaughlin, P.J., et al. (2014). The RNA-editing enzyme ADAR1 controls innate immune responses to RNA. *Cell Rep.* **9**, 1482–1494.
- Matthews, J. (2017). AHR toxicity and signaling: role of TIPARP and ADP-ribosylation. *Curr. Opin. Toxicol.* **2**, 50–57.
- Meyers, R.M., Bryan, J.G., McFarland, J.M., Weir, B.A., Sizemore, A.E., Xu, H., Dharia, N.V., Montgomery, P.G., Cowley, G.S., Pantel, S., et al. (2017). Computational correction of copy number effect improves specificity of CRISPR-Cas9 essentiality screens in cancer cells. *Nat. Genet.* **49**, 1779–1784.
- Ohmoto, A., and Yachida, S. (2017). Current status of poly(ADP-ribose) polymerase inhibitors and future directions. *Oncotargets Ther.* **10**, 5195–5208.
- Paludan, S.R., Reinert, L.S., and Hornung, V. (2019). DNA-stimulated cell death: implications for host defence, inflammatory diseases and cancer. *Nat. Rev. Immunol.* **19**, 141–153.
- Pan, D., Kobayashi, A., Jiang, P., Ferrari de Andrade, L., Tay, R.E., Luoma, A.M., Tsoucas, D., Qiu, X., Lim, K., Rao, P., et al. (2018). A major chromatin regulator determines resistance of tumor cells to T cell-mediated killing. *Science* **359**, 770–775.
- Pantelidou, C., Sonzogni, O., De Oliveria Taveira, M., Mehta, A.K., Kothari, A., Wang, D., Visal, T., Li, M.K., Pinto, J., Castrillon, J.A., et al. (2019). PARP inhibitor efficacy depends on CD8(+) T-cell recruitment via intratumoral STING pathway activation in BRCA-deficient models of triple-negative breast cancer. *Cancer Discov.* **9**, 722–737.
- Pardoll, D.M. (2012). The blockade of immune checkpoints in cancer immunotherapy. *Nat. Rev. Cancer* **12**, 252–264.
- Patro, R., Duggal, G., Love, M.I., Irizarry, R.A., and Kingsford, C. (2017). Salmon provides fast and bias-aware quantification of transcript expression. *Nat Methods* **14**, 417–419. <https://doi.org/10.1038/nmeth.4197>.
- Pattison, M.J., Mackenzie, K.F., and Arthur, J.S. (2012). Inhibition of JAKs in macrophages increases lipopolysaccharide-induced cytokine production by blocking IL-10-mediated feedback. *J. Immunol.* **189**, 2784–2792.
- Quintas-Cardama, A., Vaddi, K., Liu, P., Manshoury, T., Li, J., Scherle, P.A., Caulder, E., Wen, X., Li, Y., Waeltz, P., et al. (2010). Preclinical characterization of the selective JAK1/2 inhibitor INCB018424: therapeutic implications for the treatment of myeloproliferative neoplasms. *Blood* **115**, 3109–3117.
- Ramanjulu, J.M., Pesiridis, G.S., Yang, J., Concha, N., Singhaus, R., Zhang, S.Y., Tran, J.L., Moore, P., Lehmann, S., Eberl, H.C., et al. (2018). Design of amidobenzimidazole STING receptor agonists with systemic activity. *Nature* **564**, 439–443.
- Roder, J., and Duwe, A. (1979). The beige mutation in the mouse selectively impairs natural killer cell function. *Nature* **278**, 451–453.
- le Sage, C., Lawo, S., Panicker, P., Scales, T.M.E., Rahman, S.A., Little, A.S., McCarthy, N.J., Moore, J.D., and Cross, B.C.S. (2017). Dual direction CRISPR transcriptional regulation screening uncovers gene networks driving drug resistance. *Sci. Rep.* **7**, 17693.
- Shen, J., Zhao, W., Ju, Z., Wang, L., Peng, Y., Labrie, M., Yap, T.A., Mills, G.B., and Peng, G. (2019). PARPi triggers the STING-dependent immune response and enhances the therapeutic efficacy of immune checkpoint blockade independent of BRCAness. *Cancer Res.* **79**, 311–319.
- Soumilion, M. (2014). Characterization of directed differentiation by high-throughput single-cell RNA-seq. *bioRxiv*. <https://doi.org/10.1101/003236>.
- Vanpouille-Box, C., Hoffmann, J.A., and Galluzzi, L. (2019). Pharmacological modulation of nucleic acid sensors—therapeutic potential and persisting obstacles. *Nat. Rev. Drug Discov.* **18**, 845–867.
- Wang, B., Chu, D., Feng, Y., Shen, Y., Aoyagi-Scharber, M., and Post, L.E. (2016). Discovery and characterization of (8S,9R)-5-Fluoro-8-(4-fluorophenyl)-9-(1-methyl-1H-1,2,4-triazol-5-yl)-2,7,8,9-tetrahydro-3H-pyrido[4,3-d]phthalazin-3-one (BMN 673, talazoparib), a novel, highly potent, and orally efficacious poly(ADP-ribose) polymerase-1/2 inhibitor, as an anticancer agent. *J. Med. Chem.* **59**, 335–357.
- Wang, D., Jiang, W., Zhu, F., Mao, X., and Agrawal, S. (2018). Modulation of the tumor microenvironment by intratumoral administration of IMO-2125, a novel TLR9 agonist, for cancer immunotherapy. *Int. J. Oncol.* **53**, 1193–1203.
- Wigle, T.J., Blackwell, D.J., Schenkel, L.B., Ren, Y., Church, W.D., Desai, H.J., Swinger, K.K., Santospago, A.G., Majer, C.R., Lu, A.Z., et al. (2020b). In vitro and cellular probes to study PARP enzyme target engagement. *Cell Chem. Biol.* **27**, 877–887.e14.
- Wigle, T.J., Church, W.D., Majer, C.R., Swinger, K.K., Aybar, D., Schenkel, L.B., Vasbinder, M.M., Brendes, A., Beck, C., Prahm, M., et al. (2020a). Forced self-modification assays as a strategy to screen MonoPARP enzymes. *SLAS Discov.* **25**, 241–252.
- Yamada, T., Horimoto, H., Kameyama, T., Hayakawa, S., Yamato, H., Dazai, M., Takada, A., Kida, H., Bott, D., Zhou, A.C., et al. (2016). Constitutive aryl hydrocarbon receptor signaling constrains type I interferon-mediated antiviral innate defense. *Nat. Immunol.* **17**, 687–694.
- Zitvogel, L., Galluzzi, L., Kepp, O., Smyth, M.J., and Kroemer, G. (2015). Type I interferons in anticancer immunity. *Nat. Rev. Immunol.* **15**, 405–414.

STAR★METHODS

KEY RESOURCES TABLE

REAGENT or RESOURCE	SOURCE	IDENTIFIER
Antibodies		
Phosphorylated STAT1	Cell Signaling Technologies	Cat#9167; RRID: AB_561284
β-Actin	Cell Signaling Technologies	Cat#3700; RRID: AB_10828322
GAPDH	Cell Signaling Technologies	Cat#5174; RRID: AB_10622025
MAR/PAR	Cell Signaling Technologies	Cat#83732; RRID: AB_2749858
Phosphorylated IRF3	Cell Signaling Technologies	Cat#4947; RRID: AB_823547
IRF3	Cell Signaling Technologies	Cat#10949; RRID: AB_2797733
RIG-I	Cell Signaling Technologies	Cat#3743; RRID: AB_2269233
CGAS	Cell Signaling Technologies	Cat#15102; RRID: AB_2732795
STING	Cell Signaling Technologies	Cat#13647; RRID: AB_2732796
Anti-PD1 Clone# RPM1-14	BioXCell	Cat#BE0146; RRID: AB_10949053
Anti-IFNAR Clone# MAR1-5A3	BioXCell	Cat#BE0241; RRID: AB_2687723
Anti-mouse CD4 Clone#GK1.5	BioXCell	Cat#BE0003-1; RRID: AB_1107636
Anti-mouse CD8α Clone#2.43	BioXCell	Cat#BE0061; RRID: AB_1125541
Anti-Mouse, Rat Asialo GM1 Antibody	Wako Chemicals	Cat#986-10001; RRID: AB_516844
Anti-CD3	eBioscience	Cat#16-0031-86; RRID: AB_467048
Poly/Mono-ADP Ribose (E6F6A) mAb	Cell Signaling Technologies	Cat# 83732; RRID: AB_2749858
Goat anti-Rabbit IgG Secondary Antibody	Licor	Cat#926-32211
CD3 Clone# 145-2C11	BioLegend	Cat# 100369 ; RRID: AB_2734149
CD103 Clone# 2E7	BioLegend	Cat# 121414; RRID: AB_1227502
CD4 Clone# RM4-5	BioLegend	Cat# 100510; RRID: AB_312713
PD-1 Clone# 29F.1A12	BioLegend	Cat# 135207; RRID: AB_10550092
CD49b Clone# HMa2	BioLegend	Cat# 103506; RRID: AB_313029
CD335 Clone# REA815	Miltenyi Biotec	Cat# 130-112-359; RRID: AB_2657604
LAG-3 Clone# C9B7W	BioLegend	Cat# 125208; RRID: AB_2133343
CD45 Clone# 30-F11	BD Biosciences	Cat# 372210; RRID: AB_2728377
Granzyme B Clone# QA16A02	BioLegend	Cat# 372210; RRID: AB_2728377
FoxP3 Clone# 3G3	Miltenyi Biotec	Cat# 130-093-014; RRID: AB_871548
CD11b Clone# M1/70	BioLegend	Cat# 101215; RRID: AB_312798
CD86 Clone# GL-1	BioLegend	Cat# 105012; RRID: AB_493342)
CD80 Clone# REA983	Miltenyi Biotec	Cat# 130-116-398; RRID: AB_2727516
MHCII Clone# M5/114.15.2	eBioscience	Cat# 14-5321-82; RRID: AB_467561
CD172a (SIRPa) Clone# P84	BioLegend	Cat# 144005; RRID: AB_11204432
Siglec H Clone# 551	BioLegend	Cat# 129605; RRID: AB_1227763
CD11c Clone# N418	BioLegend	Cat# 117309; RRID: AB_313778
F4/80 Clone# BM8	BioLegend	Cat# 123116; RRID: AB_893481
PD-L1 Clone# 10F.9G2	BioLegend	Cat# 124303; RRID: AB_961230
CD206 Clone# C068C2	BioLegend	Cat# 141716; RRID: AB_2561992
CD19 Clone#1D3	BD Biosciences	Cat# 560245; RRID: AB_1645233
CD8 Clone# 53-6.7	BioLegend	Cat# 100701; RRID: AB_312740
Chemicals, peptides, and recombinant proteins		
Olaparib	AdooQ Bioscience	Cat#A1011
Niraparib	AdooQ Bioscience	Cat#A11026
Propidium iodide	Thermo Scientific	Cat#P3566
Fugene HD	Promega	Cat#E2311

(Continued on next page)

Continued

REAGENT or RESOURCE	SOURCE	IDENTIFIER
M-Per lysis buffer	Thermo Scientific	Cat#78501
HALT protease and phosphatase inhibitor	Thermo Scientific	Cat#78447
KU-60019	Selleckchem	Cat#S1570
Camptothecin	Sigma-Aldrich	Cat#C9911
Ruxolitinib	Selleckchem	Cat#S1378
BX795	Selleckchem	Cat#S1274
RBN250036	Ribon Therapeutics	This paper
RBN-2397	Ribon Therapeutics	This paper
RBN011364	Ribon Therapeutics	This paper
RBN011147	Ribon Therapeutics	This paper
RBN011198	Ribon Therapeutics	This paper
RBN011628	Ribon Therapeutics	This paper
RBN011595	Ribon Therapeutics	This paper
Mouse IFN- β	PBL Assay Science	Cat#124-001
Human IFN- β	Peprotech	Cat#500-P32B
ADU-S100	Invivogen	Cat#Tlrl-nacda2r-01
C-178	Selleckchem	Cat#S6667
RIPA lysis buffer	Millipore	Cat#20-188
SDS	Amresco	Cat#E719-100mL
T-PER lysis buffer	Thermo Scientific	Cat#78510
Pierce BCA assay	Thermo Scientific	Cat#23225
Hoechst 33342	Sigma-Aldrich	Cat#4082
RNAiMax	Thermo Scientific	Cat#13778150
1-ABT	Sigma-Aldrich	Cat#A3940
Zombie NIR viability dye	BioLegend	N/A
RoboSep Buffer	STEMCELL Technologies	Cat#20104
AHI peptide; SPSYVYHQF	GL Biochem	Cat#201905270013
β -galactosidase; TPHPARIGL	MBL International	Cat#SPM511
Matrigel	BD Biosciences	Cat#354234
Laemmli sample buffer	Bio-Rad	Cat#161-0747
TBS blocking buffer	Licor	Cat#927-60001
Poly(dA:dT)	Invivogen	Cat#tlrl-patc
Poly(I:C) (LMW)	Invivogen	Cat#tlrl-picwlv
Poly(I:C) (HMW)	Invivogen	Cat#tlrl-piclv
Lyovec	Invivogen	Cat#lyec
PARP1	Wigle et al. (2020a)	N/A
PARP2	Wigle et al. (2020a)	N/A
PARP3	Wigle et al. (2020a)	N/A
PARP4	Wigle et al. (2020a)	N/A
PARP5a	Wigle et al. (2020a)	N/A
PARP6	Wigle et al. (2020a)	N/A
PARP7	Wigle et al. (2020a)	N/A
PARP8	Wigle et al. (2020a)	N/A
PARP9	Wigle et al. (2020a)	N/A
PARP10	Wigle et al. (2020a)	N/A
PARP11	Wigle et al. (2020a)	N/A
PARP12	Wigle et al. (2020a)	N/A
PARP13	Wigle et al. (2020a)	N/A

(Continued on next page)

Continued

REAGENT or RESOURCE	SOURCE	IDENTIFIER
PARP14	Wigle et al. (2020a)	N/A
PARP15	Wigle et al. (2020a)	N/A
PARP16	Wigle et al. (2020a)	N/A
Biotin-NAD ⁺	Biolog	Cat. # N012

Critical commercial assays

QuantiGene Singleplex HT Assay kit	Thermo Scientific	Cat#QS0384
Cell TiterGlo	Promega	Cat#G7573
β-Galactosidase activity	Cell Signaling Technologies	Cat#9860
2'3'-cGAMP ELISA assay kit	Cayman Chemical	Cat#501700
Qiagen RNeasy Plus Mini Kit	Qiagen	Cat#74136
MagMAX-96 for microarrays total RNA isolation kit	Thermo Scientific	Cat#AM1839
Miltenyi Tumor Dissociation Kit	Miltenyi	Cat#130-096-730
SSVLO Reverse Transcription kit	Omni International	Cat#11754-250
Taqman multiplex Master Mix	Thermo Scientific	Cat#4461882
CXCL10/IP-10 Quantikine ELISA Kit	R&D Systems	Cat#DIP100
Mouse CD3+ T Cell Isolation Kit	STEMCELL Technologies	Cat#19851A
Mouse IFN-γ ELISpot Kit	MABTECH	Cat#3321-2A
QuantiGene Singleplex HT Assay Kit	Thermo Scientific	Cat#QS0384
Europlum-labeled streptavidin	Perkin Elmer	Cat. # AD0063
ULight-labeled streptavidin	Perkin Elmer	Cat. # AD0062
Europlum-labeled anti-His	Perkin Elmer	Cat. # AD0111
Ulight-labeled anti-His	Perkin Elmer	Cat. # TRF0105
384-well nickel-NTA coated microplates	Thermo	Custom
DELFIa Eu-N1 Streptavidin	Perkin Elmer	Cat. # 1244-360
DELFIa Assay Buffer	Perkin Elmer	Cat. # 1244-111
DELFIa Enhancement Solution	Perkin Elmer	Cat. # 1244-105
IntracellularTE Nano-Glo(R) Substrate/Inhibitor	Promega	Cat. # N2161
DELFIa Enhancement Solution	Perkin Elmer	Cat. # 1244-105

Deposited data

Structure of PARP12 mutant bound to RBN-2397	This paper	PDB: 6V3W
RNA-seq dataset	This paper	GEO:GSE177494; https://www.ncbi.nlm.nih.gov/geo/query/acc.cgi?acc=GSE177494
CRISPRi/a dataset	This paper	GEO: GSE178386; https://www.ncbi.nlm.nih.gov/geo/query/acc.cgi?acc=GSE178386
R scripts	This paper	https://github.com/cl-ribon/parp7_cancercell

Experimental models: cell lines

4T1	ATCC	CRL-2539
A20	ATCC	TIB-208
B16-F10	ATCC	CRL-6475
BEAS-2B	ATCC	CRL-9609
CAL27	ATCC	CRL-2095
HCC827	ATCC	CRL-2868
HPAF-II	ATCC	CRL-1997
KLN205	ATCC	CRL-1453
NCI-H1373	ATCC	CRL-5866
NCI-H1373 Cas9 overexpressing clone	Ribon Therapeutics	NA
NCI-H1703	ATCC	CRL-5889
NCI-H1944	ATCC	CRL-5907
NCI-H2066	ATCC	CRL-5917

(Continued on next page)

Continued

REAGENT or RESOURCE	SOURCE	IDENTIFIER
NCI-H2347	ATCC	CRL-5942
NCI-H596	ATCC	HTB-178
NCI-H647	ATCC	CRL-5834
NCI-H226	ATCC	CRL-5917
PANC03.27	ATCC	CRL-2549
PANC-1	ATCC	CRL-1469
MRC-5	ATCC	CCL-171
RENCA	ATCC	CRL-2947
SK-MES	ATCC	HTB-58
HEK-293T	ATCC	CRL-3216
CT26	ATCC	CRL-2638
CT26-Cas9	Genecopoeia	Cat# SL582
COR-L105	MilliporeSigma ECACC	92031918
HARA	JCRB	JCRB1080.0
HCC-44	DSMZ	ACC 534
SCC-25	DSMZ	ACC 617
HCC95	KOREAN CELL LINE BANK	70095
MOC1	WASHINGTON UNIVERISTY	N/A
MOC2	WASHINGTON UNIVERISTY	N/A
UN-SCC680AJ	FUNDACION PARA LA INVESTIGACION MEDICA APLICADA	N/A

Experimental models: organisms/strains

CB17 female mice	Beijing Vital River Laboratory Animal Technology Co., Ltd	404
Beige SCID female mice	Beijing Vital River Laboratory Animal Technology Co., Ltd	405
BALB/c female mice	Shanghai Lingchang Biotech Co. Ltd.	N/A
Athymic Nude-Foxn1nu female mice	Envigo, Indianapolis, Indiana	N/A

Oligonucleotides

Cherry-picked Edit-R crRNA library	Horizon Discovery	N/A
IFN- β gene primers forward (ATGACCAACAAGTGTCTCCTCC) reverse (GCTCATGGAAAGAGCTGTAGTG)	Integrated DNA technology	N/A
CRISPR targeting sequences; see Table S8	Dharmacon	N/A
CRISPR KO targeting sequences for CT26 and NCI-H1373 KO cell lines; see Table S8	Canopy	N/A
Taqman primer/probe sequences; see Table S8	Thermo Scientific	N/A

Recombinant DNA

pLVX-IRES-pur plasmid	Clontech	Cat#632183
Plasmid: CAG-Blast-Cas9 Nuclease	Dharmacon	Cat#VCAS10129

Software and algorithms

MetaXpress 6	Molecular Devices	https://www.moleculardevices.com/products/cellular-imaging-systems/acquisition-and-analysis-software/metaxpress#graf
GraphPad Prism 8	GraphPad Software	https://www.graphpad.com/scientific-software/prism/
MAGeCK v0.5.0	Cross et al., 2016 Li et al., 2014	https://sourceforge.net/p/mageck/wiki/Home/

(Continued on next page)

Continued		
REAGENT or RESOURCE	SOURCE	IDENTIFIER
Robust Rank Aggregation (v1.1)	Kolde et al., 2012	https://rdrr.io/cran/RobustRankAggreg/
R statistical software v3.6.1	The R Foundation	https://www.r-project.org/
fgsea v1.10.19	Sergushichev et al., 2016	https://bioconductor.org/packages/fgsea/
DESeq2 v1.18.18	Love et al.,(2014)	https://bioconductor.org/packages/release/bioc/html/DESeq2.html
Salmon v0.11.27	Patro et al., (2017)	https://combine-lab.github.io/salmon/
Other		
Cytosolic DNA detection	intoDNA Kordon et al., 2020	N/A
Custom 100 gene nanoString array	NanoString	N/A
Odyssey CLx	LI-COR biosciences	N/A
Bead Ruptor Elite	Omni International	Cat#19-040E
ImgaXpress Micro XLS	Molecular Devices	N/A
Elispot reader	AID	Cat#9207233
Mini-PROTEAN TGX Gel	Bior-Rad	Cat#4561096
CRISPRi/a screen	Horizon Discovery le Sage et al., 2017	N/A

RESOURCE AVAILABILITY

Lead contact

Further information and requests for resources and reagents should be directed to and will be fulfilled by the lead contact, Joseph Gozgit (jgozgit@ribontx.com).

Materials availability

All unique/stable reagents generated in this study are available from the lead contact with a completed Materials Transfer Agreement.

Data and code availability

RNA-seq and CRISPRi/a data have been deposited at GEO and are publicly available as of the date of publication. Accession numbers are listed in the [key resources table](#). All analysis code has been deposited at GitHub (https://github.com/cl-ribon/parp7_cancercell) and is publicly available as of the date of publication. X-ray crystallographic coordinates and structure factor files have been deposited in the Protein Data Bank (PDB: 6V3W).

EXPERIMENTAL MODEL AND SUBJECT DETAILS

Mouse strains

The following mouse strains were used in these studies: CB17 female, Beige SCID female (Beijing Vital River Laboratory Animal Technology Co., Ltd), BALB/c (Shanghai Lingchang Biotech Co. Ltd.) and Athymic Nude-Foxn1nu female mice (Envigo, Indianapolis, Indiana). All mice were 6–8 weeks of age for efficacy and PK/PD studies. Mice were 16–21 week of age for re-challenge studies.

Cell lines

4T1, A20, B16-F10, BEAS-2B, Cal27, HCC827, HPAF-II, KLN205, NCI-H1373, NCI-H1703, NCI-H1944, NCI-H2066, NCI-H2347, NCI-H596, NCI-H647, NCI-H226, Panc 03.27, Panc 08.13, PANC-1, MRC-5, RENCA, SK-MES, HEK-293T and CT26 were purchased from American Type Culture Collection (ATCC, Manassas, VA). COR-L105 was purchased from European Collection of Authenticated Cell Cultures (MilliporeSigma, Burlington, MA). HARA was purchased from the JCRB Japanese Collection of Research Bioresources Cell Bank (JCRB, Osaka, Japan). HCC-44 and SCC-25 were purchased from the German Collection of Microorganisms and Cell Cultures (DSMZ, Braunschweig, Germany). EBC-1 was purchased from the Riken Cell Bank (Tsukuba, Ibaraki, Japan). HCC95 was purchased from the Korean Cell Line Bank (Seoul, South Korea). MOC1 and MOC2 were obtained from The Washington University (St. Louis, MO) and UN-SCC680AJ were obtained from Fundacion para la Investigacion Medica Aplicada (Pamplona, Spain). All cell lines were maintained according to the data sheets provided by the individual cell banks.

METHOD DETAILS

TCGA and dependency map analysis

TCGA gene expression data were extracted from Genomics Data Commons Portal using the HTSeq – Counts workflow analysis. TCGA copy-number analysis data were extracted from the Broad Institute TCGA GDAC GISTIC2 SNP6 Copy number analysis (28 January 2016 release).

The publicly available human cancer cell line processed CRISPR dependency data (Meyers et al., 2017); (Dempster et al., 2019) (Achilles dataset 20Q2) was downloaded from the Dependency Map web portal (depmap.org). The Achilles dataset contains genome-scale CRISPR knockout screens for 18,119 genes in 769 cell lines (Meyers et al., 2017; Dempster et al., 2019).

Surface plasmon resonance (SPR)

The binding affinity of RBN-2397 was measured using SPR. PARP7 was expressed and purified as previously described (Wigle et al., 2020a). Further details on this methodology are included in the [supplemental information](#).

Biochemical PARP inhibition assays

PARP enzymes were made and run in enzyme inhibition assays as previously described (Wigle et al., 2020b). Displacement of a biotinylated compound (RBN011147) binding to the active sites of His-tagged PARP7, PARP14 and PARP16 was measured using a time-resolved fluorescence energy transfer (TR-FRET) assay where acceptor and donor fluorophores are captured onto the biotin and His tags. Further details on this methodology are included in the [supplemental information](#).

MAR/PAR in-cell western (ICW) assay

The inhibition of PARP7 enzymatic activity in cells was determined by using an ICW assay to measure immunofluorescent staining of global MARylation in SK-MES-1 cells stably transfected with doxycycline-inducible full-length PARP7 (SK-MES-1 PARP7-OE). Further details on this methodology are included in the [supplemental information](#) (Lu et al., 2019).

Active site probe displacement NanoBRET assay

Displacement of a fluorescently labeled compound (RBN011198) binding to the active site of NanoLuc-tagged full-length PARP7 expressed in 293T cells was measured using a NanoBRET Target Engagement assay (Promega, Madison, WI) as previously described (Wigle et al., 2020b). Further details on this methodology are included in the [supplemental information](#).

RNA detection assay for PARP7-mediated CYP1B1 RNA regulation

The modulation of *CYP1B1* mRNA levels by PARP7 was measured using the QuantiGene Singleplex HT Assay kit (Thermo Scientific, QS0384). Further details on this methodology are included in the [supplemental information](#).

Cell proliferation

Cells were seeded at previously optimized seeding densities in two 384-well white-walled tissue culture-treated plates and either treated immediately or allowed to adhere overnight, depending on the cell line. Cell viability was measured immediately after dosing (Day 0) and after 6 days of incubation using Cell TiterGlo (CTG, Promega, G7573). The Day 0 average luminescence value was subtracted from individual Day 6 values before analyzing the plate for percent of control (DMSO). GI₅₀s for each compound were calculated by non-linear regression analysis (4-parameter fit) and geometric means were calculated across runs. Olaparib and niraparib were purchased from AdooQ Bioscience (Irvine, CA).

Cancer cell line screen

A broad cancer cell line screen was performed at Horizon Discovery (Cambridge, UK) using similar methodology as described above. A four-parameter logistic model was applied to model the relationship between compound dose level and cellular growth using R statistical package dr4pl v1.1.7.1. Further details on these analyses are included in the [supplemental information](#).

Cell cycle and senescence assays

NCI-H1373 cells were treated with RBN-2397 for 3 days, harvested, and then fixed and permeabilized in 70% EtOH. Cells were then stained with 50 μ g/mL propidium iodide (Thermo Scientific, P3566) and analyzed by flow cytometry on a Cytoflex flow cytometer. FACS data was analyzed using Flowjo software. For the senescence assay, cells were seeded and allowed to attach overnight, and treated with RBN-2397 for 6 days. Senescence was detected by staining for β -Galactosidase activity (Cell Signaling Technologies, 9860) according to manufacturer's instructions. Images were captured on a Nikon ECLIPSE TS100 phase contrast microscope.

PARP7 overexpression

HEK293T cells were transfected with the pLVX-IRES-puro plasmid containing full-length human PARP7 with an N-terminal 3 x Hemagglutinin (HA) Tag or empty vector (Clontech, 632183) using the Fugene HD transfection reagent (Promega, E2311) according to manufacturer's instructions. 48 hours post transfection, cells were then treated with LyoVec (#lyec-12) control or 1 g/mL poly(dA:dt)

(#tlrl-piclv, Invivogen, San Diego, CA) for 24 hr. RNA was extracted from cells and IFN- β gene expression was determined by QPCR using forward (ATGACCAACAAGTGTCTCCTCC) and reverse (GCTCATGGAAAGAGCTGTAGTG) primers (Integrated DNA Technology, Coralville, Iowa).

2'3'-cGAMP ELISA

Cells were rinsed with ice-cold PBS and scraped with cold M-Per lysis buffer (ThermoFisher Scientific, 78,501) supplemented with HALT protease and phosphatase inhibitor (ThermoFisher, #78447) 24 hr after treatment with DMSO or 2 μ M KU-60019 (Selleckchem, S1570). 2'3'-cGAMP was measured in cell lysates with a competitive ELISA assay kit (Cayman Chemical, 501700) according to manufacturer's instructions.

Cytosolic DNA detection

Cytosolic DNA detection and analysis were performed by intoDNA (Krakow, Poland). Cells were seeded at subconfluent densities onto round glass coverslips (thickness 0.17 mm, diameter 15 mm) and fixed with 70% (v/v) ethanol at -20°C overnight. Following fixation, for the purpose of detection of DNA fragments in the cytoplasm, the cells underwent procedures of SensiTive Recognition of Individual double-strand DNA Ends (dSTRIDE) as previously described (Kordon et al., 2020). Treatment of NCI-H1373 cells with 1 μ M camptothecin (Sigma-Aldrich, C9911) or DMSO for 24 hr served as controls for the assay.

Transfection of PRR ligands

PRR ligand transfection was performed using LyoVec (Invivogen #lyec-12), poly(dA:dT) (Invivogen # tlr-patc) as double-stranded DNA or a 1:1 mixture of low molecular weight (Invivogen # tlr-picwlv) and high molecular weight poly(I:C) (Invivogen # tlr-piclv) as double-stranded RNA according to the manufacturers' instruction. NCI-H1373 cells were transfected with PRR ligands at the final concentration of 0.1 $\mu\text{g}/\text{mL}$, and cells were co-treated with 1 μ M RBN-2397 or vehicle control for 24 hr before immunofluorescent assays were performed.

nanoString analysis

Cells were plated at a density of 1.5×10^6 cells/well in 6-well dishes and allowed to adhere overnight prior to 24 hr of compound treatment. Media was removed and cells were rinsed with phosphate buffered saline (PBS) before being pelleted and frozen. RNA was isolated using Qiagen RNeasy Plus Mini kit (Qiagen, #74136) and ran on a custom 100 gene nanoString array per standard protocol (Canopy Biosciences, St. Louis, MO). Standard nanoString quality control and normalization measures were applied to the raw expression data (see https://www.nanostring.com/download_file/view/251/8241). Normalized expression values were compared between treatment and control samples to obtain log-transformed fold-change values. Visualized log-transformed values were plotted in a heatmap with data-driven row and column clustering using R package ComplexHeatmap v1.17.1 (Gu et al., 2016).

RNA sequencing

Cells were plated at a density of 1.5×10^6 cells/well in 6-well dish and allowed to adhere overnight prior to compound treatment. Cells were harvested after either 6 or 24 hr of treatment. RNA was isolated using the MagMAX-96 for Microarrays Total RNA Isolation Kit (Thermo Fisher Scientific, #AM1839) per manufacturer's instructions. RNA concentration was determined using a NanoDrop 8000 (ThermoFisher Scientific, Waltham, MA). Paired-end sample libraries consisting of 60 bp with 6 nucleotide indices were prepared for measuring high-throughput 3' digital gene expression based on a previously published protocol (Massachusetts Institute of Technology, Cambridge, MA) (Soumillon, 2014). Further details on this methodology are included in the [supplemental information](#).

Western blotting

For *in vitro* assays, cells were plated at a previously optimized density and allowed to adhere overnight prior to treatment with RBN-2397 (1 μ M, unless otherwise stated). Other treatments included ruxolitinib (1 μ M, Selleckchem, S1378), BX795 (1 μ M, Selleckchem, S1274), RBN250036 (Ribon Therapeutics), mouse (10 ng/mL PBL Assay Science, #12400-1) or human interferon-beta (10 ng/mL Peprotech, #500-P32B), ADU-S100 (Invivogen, tlr-nacda2r-01), or C-178 (Selleckchem, S6667) (Haag et al., 2018). After 24 hr of treatment, cells were rinsed with PBS on ice prior to being scrapped in RIPA lysis buffer (Millipore, #20-188) supplemented with 0.1% sodium dodecyl sulfate (SDS, Amresco, E719-100mL) and HALT protease and phosphatase inhibitor (ThermoFisher, #78447). For *in vivo* samples, frozen tumors were weighed and 50 mg of each sample was placed in homogenate tubes containing beads (VWR, #10032-756) with T-PER lysis buffer (Thermo, #78510), supplemented with Halt protease and phosphatase inhibitor. Samples were homogenized using a Bead Ruptor Elite (Omni International, #19-040E). All clarified lysates were assayed for protein concentration by Pierce BCA assay (ThermoFisher, #23225) per kit instructions. Blots were incubated with appropriate antibodies and imaged on an Odyssey CLx (LI-COR Biosciences, Lincoln, NE). Antibodies were obtained from the following sources: phosphorylated STAT1 (#9167); STAT1 (#9176); β -ACTIN (#3700); GAPDH (#5174); MAR/PAR (#83732); phosphorylated IRF3 (#4947), IRF3#10949), RIG-I (#3743); cGAS (#15102); STING (#13647, Cell Signaling Technology); IRDye 680RD Donkey anti-Mouse IgG (LI-COR Biosciences, #926-68022); IRDye 800CW Goat anti-Rabbit IgG (LI-COR Biosciences, #926-32211). Analysis was performed with Odyssey Image Studio (LI-COR Biosciences, Lincoln, NE).

Immunofluorescence staining and imaging

NCI-H1373 cells were plated at a density of 2×10^3 cells/well in 384-well plates and treated with $1 \mu\text{M}$ RBN-2397 for 24 hr. After treatment, the cells were fixed with ice-cold methanol for 20 min at -20°C and permeabilized with 0.5% Triton X-100 for 15 min at room temperature. After incubating with blocking buffer (LI-COR Biosciences, 927-50,010), cells were stained with either pSTAT1 (CST, #9167) or pIRF3 (CST #29047), followed by incubation with secondary antibody (ThermoFisher, A32733) and Hoechst 33,342 (Sigma, #4082). Images were acquired on an ImageXpress Micro XLS (Molecular Devices, San Jose, CA) and analyzed with MetaXpress 6 (Molecular Devices, San Jose, CA). Average nuclear intensity was measured and further blanked with non-primary staining controls to quantify the pSTAT1 level. Statistics analysis was performed with unpaired *t*-tests using GraphPad Prism 8 (GraphPad Software, La Jolla, CA).

CRISPRi/a screen

CRISPR-Cas9 dual screening with RBN-2397 (2.5 nM) in NCI-H1373 cells was performed at Horizon Discovery (Cambridge, UK). Briefly, cells were transduced with either whole-genome CRISPR activation (CRISPRa) or interference (CRISPRi) libraries, then selected and maintained in culture to allow CRISPR-driven gene perturbations to occur (le Sage et al., 2017). Further details on this methodology are included in the [supplemental information](#).

CRISPR gene KO

A clone of Cas9 overexpressing NCI-H1373 cells was established by transduction with Cas9 lentivirus (Dharmacon, VCAS10129) following the instruction of Collecta CRISPR library user manual (v2). Transient gene knockouts were performed in Cas9 expressing cells with crRNA:tracrRNA transfection using RNAiMax (ThermoFisher, #13778150) according to the manufacturer's instructions. In brief, NCI-H1373 Cas9 overexpressing cells were transfected with crRNA:tracrRNA with the final concentration of 25 nM. Each gene was targeted by a pool of three crRNAs (Dharmacon, see [supplemental information](#)). Forty-eight hours post transfection, cells were treated with PARP7 inhibitor or DMSO for another 5 days. Relative growth inhibition of gene-edited cells was calculated by subtracting the Day 0 values, followed by normalizing to DMSO controls. Dose-response curves were generated with non-linear regression analysis (3-parameter fit) and statistical analyses were performed with extra sum-of-squares F tests, using GraphPad Prism 8.

CRISPR arrayed screening

Arrayed CRISPR screens were conducted using a cherry-picked Edit-R crRNA library (Horizon Discovery, Cambridge, UK) targeting 234 innate immunity-related genes and 6 non-targeting or intron-targeting negative controls in Cas9-expressing NCI-H1373 cells. Further details on this methodology are included in the [supplemental information](#).

Generation of CRISPR KO CT26 cells

CT26 TBK1, IFNAR1, PARP1 and PARP7 KO cell lines were generated at Canopy Biosciences (St. Louis, MO). CRISPR-Cas9 was used to knockout mTBK1 and mIFNAR1 in CT26 cells via introduction of frame shifting insertions/deletions (indels) via non-homologous end-joining (NHEJ). Briefly, crRNAs were designed targeting exon 5 of mouse TBK1 and exon 4 of mouse IFNAR1. In silico screens for predicted activity and potential off-target effects, and the highest scoring designs were synthesized. The crRNAs were nucleofected into CT26 cells along with tracrRNA and Cas9 protein. The nucleofected pools were screened via next generation sequencing for Cas9 activity, and the pools were single cell sorted. The clones were expanded and sequenced. Sequencing data confirmed biallelic knockout of mouse genes ([Table S7](#)).

Substrate ID by mass spectrometry

Cell lysis, immunoprecipitation, and mass spectrometry analysis methods were performed as previously described (Lu et al., 2019).

In vivo studies

Multiple efficacy and single-dose PK/PD studies using human cancer cell lines were performed in CB17 or Beige SCID female mice (Chempartner, Shanghai, China) while the CT26 syngeneic model studies were performed in BALB/c female mice (Chempartner, Shanghai, China). Studies were conducted using the following compounds: RBN-2397 (oral gavage once a day at the indicated schedule; RBN-2397 was co-formulated with 1-ABT to increase exposure (50 mg/kg, 1-ABT, Sigma, #A3940, CAS# 1614-12-6) for selected CT26 BALB/c studies, as indicated); 5 mg/kg of Anti-PD-1 (intraperitoneal injection, twice a week (BIW) at the indicated schedule, delivered in a volume of 0.2 mL/20 g mouse (10 mL/kg) and adjusted for the last recorded weight of the individual animals; BioXCell, # BE0146, Clone# RMP1-14); 200 μg Anti-IFNAR antibody (intraperitoneal injection, BIW for 3 weeks, BioXCell, Cat# BE0241, Clone# MAR1-5A3). For all studies, tumor volumes were determined by manual calipers every 2-3 days. The tumor volumes were then used for the calculations of tumor growth inhibition (TGI) and tumor regression rate (TR). Summary statistics including mean and standard error of the mean (SEM) were calculated for the tumor volumes of each group at each time point. Statistical analyses for TGI were performed when at least 8 of the 10 mice were remaining in the vehicle group. Two-way ANOVAs followed by Bonferroni post-tests were performed to compare tumor volumes at different days between groups. All statistical and graphical analyses were performed with GraphPad Prism version 8. Further details on this methodology are included in the [supplemental information](#).

PDX studies

Patient derived xenograft (PDX) studies were performed at Champions Oncology (Rockville, MD) using Athymic Nude-Foxn1nu female mice (Envigo, Indianapolis, Indiana). Tumors were grown in stock mice until they reached approximately 1.0–1.5 cm³, tumors were then harvested for re-implantation into pre-study animals. Pre-study animals were implanted unilaterally on the left flank with tumor fragments. Pre-study tumor volumes were recorded for each experiment beginning seven to ten days after implantation. Mice were randomized when tumors reached an average tumor volume of 150–300 mm³ and dosing initiated on Day 0. Mice were daily administered either vehicle (50% Labrasol) or RBN-2397 500 mg/kg QD. Tumors were measured twice a week. The tumor volumes were then used for the calculations of tumor growth inhibition (TGI). Data are plotted as mean ± standard error of the mean (SEM). Study was conducted as a screen and only included 3 mice per group.

Tumor re-challenge

For CT26 BALB/c studies, tumor-free mice were monitored for 60 days following the dosing period. Tumor-free mice were re-challenged with either CT26 or 4T1 cells inoculated on the opposite flank from the original tumor. naive mice were used as controls.

In vivo immune depletion

CT26-tumor bearing BALB/c mice (mean tumor size 70–80 mm³) were administered with either vehicle or RBN-2397 (100 mg/kg QD) co-formulated with 1-ABT (50 mg/kg) starting on day 1 of a 28-day efficacy study (Covance, Ann Arbor, MI). CD4 and CD8 T cells were depleted using 4 consecutive doses of GK1.5 and 2.43 antibodies (200 µL/dose, Bio X Cell), respectively, on day 0 (staging day), day 1, day 2, and day 6. NK cells were depleted using 6 consecutive doses of anti-AsGM1 (50 µL/dose, Wako Chem) on day –7 (2 days before cell implantation), day –5 (implantation day), day 0, day 1, day 2, and day 6. Changes in immune cell numbers were determined by flow cytometry analysis in both blood and tumor on day 9 using the panels described in [supplemental information](#) and counting beads.

Immunophenotyping

CT26-tumor bearing BALB/c mice (mean tumor size 81 mm³) were administered either vehicle or RBN-2397 (500 mg/kg QD) and tumors were harvested on days 3, 6 and 12 for immunophenotyping by flow cytometry (Covance Ann Arbor, MI). For analysis of immune cell populations, isolated tumors were weighed and dissociated using the Miltenyi Tumor Dissociation Kit (Miltenyi, 130-096-730). Samples were washed through a 70 µM cell strainer followed by centrifugation and red blood cell lysis. Tumor cells were blocked with CD16/32 and stained with Zombie NIR viability dye (BioLegend). Cells were washed and stained with respective antibody panels and acquired. All samples were acquired on an Attune NxT flow cytometer, and data were analyzed using FlowJo software (Becton Dickinson, Franklin Lakes, NJ). Further details on antibody reagents are included in [supplemental information](#). Gating strategy is shown in [supplemental information](#).

Quantitative PCR (qPCR)

RNA harvest and isolation for qPCR was performed using the MagMAX-96 for Microarrays Total RNA Isolation Kit (Thermo Fisher Scientific, #AM1839) per manufacturer's instructions. In brief, frozen tumors were weighed and 50 mg was placed in homogenate tubes containing beads (VWR, #10032-756) with 700 µL of Tri-reagent. Samples were homogenized using a Bead Ruptor Elite (Omni International, #19-040E). RNA was further purified using the KingFisher Flex (ThermoFisher Scientific, Waltham, MA). RNA concentration was determined using a NanoDrop 8000. Reverse transcription of the RNA was carried out using the SSVILO Reverse Transcription kit (ThermoFisher, # 11,754-250) per manufacturer's instructions. qPCR reactions were performed in a LightCycler 480 (Roche Life Science) in 384-well white-walled qPCR plates (USA Scientific, #1438-1690) using Taqman Multiplex Master Mix (ThermoFisher, #4461882).

CXCL10 ELISA

Xenograft tumors were processed as described in the Western blotting method section for *in vivo* samples. CXCL10 protein level was determined with the human CXCL10/IP-10 Quantikine ELISA Kit (R&D Systems, DIP100) and absorbance was measured using the EnVision plate reader from PerkinElmer per manufacturer's instructions. Analysis was performed with the SOFTMAX PRO software.

Ex vivo T cell response using IFN- γ ELISPOT

CT26-tumor bearing BALB/c mice were administered RBN-2397 (100 mg/kg co-dosed with 50 mg/kg 1-ABT, QD) and spleens were harvested on day 15 for *ex vivo* analysis (Chempartner, Shanghai, China). Spleens from tumor-bearing mice were pressed through 70 µM nylon cell strainers to generate single cell suspensions in cold PBS. Splenocytes were isolated from RBC using Ficoll separation. Splenocytes were centrifuged and re-suspended in RoboSep™ Buffer (STEMCELL Technologies, #20104) and T cells were isolated using Mouse CD3⁺ T cell Isolation Kit (EasySep, #19851A, negative enrichment for T cells). Spleens from 2 normal healthy naive BALB/c mice (pooled sample, 8 week old female mice) were used as controls. 5 × 10⁴ T cells in RPMI-1640 with 10% FBS together with syngeneic spleen cells (1:1 ratio) were plated per well (in triplicate) and stimulated with AH1 (0.5 mM, SPSVYVHQF) peptide (GL Biochem, # 201905270013) or β -galactosidase (100 µg/mL, TPHPARIGL) peptide (MBL International, #SPM511). Control wells for all conditions were set up with no antigenic stimulus or anti-CD3 (1 µg/mL, eBioscience, #16-0031-86) as a positive control

and incubated at 37°C with 5% CO₂ for 24 hr. Spots were developed using the Mouse IFN- γ ELISpot kit (MABTECH, #3321-2A) according to manufacturer's instructions. The number of spots were measured by Elispot reader (AID, 9207233).

QUANTIFICATION AND STATISTICAL ANALYSIS

All statistical details for the experiments can be found in the figure legends. For *in vitro* studies including acute CRISPR, cell cycle and gene expression, p values were determined by a two-tailed Student's t-test or one-way ANOVA depending on group size. For acute CRISPR proliferation studies (Figure S6A and S6B), p values were determined by extra sum-of-squares F test. For *in vivo* studies, statistical analyses for TGI were performed when at least 80% of the mice were remaining in the vehicle group. p values for efficacy or PD were determined by either two-tailed Student's t-test for two groups or a two-way ANOVA with multiple comparisons for studies with more than 2 groups. Significant changes in IFN- γ producing splenic T cells were determined with a one-sided Mann Whitney U Test. All statistical analyses listed above were performed using GraphPad Prism 8. For the human cell line screen, a four-parameter logistic model was applied to determine the relationship between compound dose level and cellular growth using R statistical package dr4pl v1.1.7.1. For RNAseq, differentially expressed genes between treatment and control samples were identified with R package DESeq2 v1.18.1. Significant gene expression changes defined by the false discovery rate (FDR) < 0.05 and fold-change > 2. Geneset enrichment analysis was performed using R package fgsea v1.10.1. For TCGA analysis, significant correlations were determined by Spearman rank correlation coefficients calculated in R statistical software v3.6.1.